Ocean Engineering 305 (2024) 117874

Contents lists available at ScienceDirect

Ocean Engineering

journal homepage: www.elsevier.com/locate/oceaneng

# Mechanically coupled wave farms: On the accuracy of a mid-fidelity hydrodynamic model under consideration of varying calibration approaches

Jannik Meyer [a,*], Christian Windt [b], Arndt Hildebrandt [a], Torsten Schlurmann [a]

[a] University of Hannover, Ludwig-Franzius-Institute, Nienburger Strasse 4, Hannover, D-30167, Germany
[b] Technische Universität Braunschweig, Leichtweiß-Institute for Hydraulic Engineering and Water Resources, Beethovenstrasse 51a, Braunschweig, D-38106, Germany

ARTICLE INFO

*Keywords:*
Numerical modeling
Experimental modeling
Point absorber array
WEC-Sim
Wave energy
BEM

ABSTRACT

The early stages of wave farm design require many parametric studies, e.g., regarding geometrical optimization of the array layout. Hence, mid-fidelity numerical models are employed due to their computational efficiency. In this study, the accuracy of these models and the necessary quality of input data (e.g., from Boundary Element Method simulations) is investigated using different calibration approaches. A heaving point absorber array comprising 24 devices, which are connected using a rigid frame, is used as the example wave farm. Three different approaches of model calibration are compared: (i) a low-effort approach without any calibration of the input data; (ii) an approach with medium-effort calibration based on experimental data of a single point absorber; and (iii) an approach with high-effort calibration based on experimental data of a whole wave farm. After a comparison with experimental data, the wave farm's power output using the three approaches is calculated and the accuracy as well as the implications for further design stages are discussed. The mid-fidelity hydrodynamic model can reproduce the mechanical interactions in the wave farm accurately, while the medium effort calibration shows high applicability due to the strong influence of the single point absorber calibration on the wave farm's power output.

## 1. Introduction

The international community is aiming at the mitigation of climate change by reducing greenhouse gas emissions. Global emission targets are outlined in the Paris Agreement, which was adopted in 2015 and ratified in 2016. Most countries work towards reaching emission reductions by replacing fossil energy sources with renewable alternatives in various economic sectors, e.g., mobility and heating. This leads to a growing demand for clean electricity. While some sources of renewable energy like wind energy, solar energy, and hydropower are already well established, the harvesting of ocean energy by tidal or wave energy plants is not. Nonetheless, ambitious aims are set by some governing bodies. E.g., the European Union has the goal of 1 GW installed ocean energy capacity for 2030 and 40 GW installed ocean energy capacity for 2050 (European Commission, 2020).

To reach these ambitious goals, further development is necessary in both the tidal and the wave energy sector. The potential of wave energy conversion is undisputed due to the large wave energy resource. Several estimations of global wave energy resource exist, most laying between 2 TW and 4 TW (e.g., 2.11 TW (Gunn and Stock-Williams, 2012) or 3.7 TW (Mork et al., 2010)). High wave energy potential is found especially in the areas between the latitude of 40° and 60° on both hemispheres (Rusu and Rusu, 2021). However, still no commercially feasible wave energy converter (WEC) exists. To reach the next steps in wave energy commercialization, synergies with other offshore technologies due to hybridization or co-location (multi-use) should be searched, or niche markets should be aimed for instead of competing with much more mature technologies like wind or solar energy (Clemente et al., 2021).

In recent years, point absorber (PA) WECs became the dominating device type compared to oscillating water column (OWC) and overtopping devices (OTD) (He et al., 2023). Due to the small sizing of a single PA device, these will have to be installed in wave farms to reduce capital and operational expenditures (CAPEX and OPEX), e.g., by sharing grid connection.

During the development process of a WEC and a wave farm, different levels of technology development have to be reached. These can be described by the metrics Technology Readiness Level (TRL) and Technology Performance Level (TPL). Weber (2012) defines the TPL as a measure of a WEC's economic ability, i.e., the cost of energy for a system with a high TPL is low and vice versa. On the other hand,

* Corresponding author.
*E-mail address:* meyer@lufi.uni-hannover.de (J. Meyer).

https://doi.org/10.1016/j.oceaneng.2024.117874
Received 27 January 2024; Received in revised form 22 March 2024; Accepted 10 April 2024
Available online 24 April 2024

the TRL is defined as a measure of a WEC's commercial ability, i.e., the necessary future development cost for a WEC with low TRL is large and vice versa. Combining both measures into a TRL-TPL-matrix – or a WEC technology map – different development trajectories can be discussed. Aiming at a high TRL before focusing on the increase of the TPL is called *readiness before performance* while increasing the TPL before rising the TRL is called *performance before readiness*. Weber (2012) proposes an improved realistic development trajectory following the latter principle. In the initial design stages with low TRL, the WEC's system fundamentals are still flexible and an increase in TPL should be aimed at. After reaching sufficient TPL, the system fundamentals are fixed and TRL can be increased by further refinement of the technology. Before the definition of the TPL concept, Nielsen (2010) proposed to divide the WEC development process into different stages. The first two stages comprise concept validation (stage 1, TRL 1–3) and design validation (stage 2, TRL 4). In both stages, various flume tests on small and intermediate scales are proposed, in combination with numerical modeling. At the end of stage 2, a rough estimate of the annual energy production (AEP) and the cost of energy should be calculated. Hence, these first two phases focus on the operational state of the device, while survivability is of secondary importance. Both presented development approaches give similar recommendations, focusing on optimizing the WEC with still flexible system fundamentals with medium-effort approaches (e.g., small- to medium-scale model tests, numerical simulations) while TRL is low and refining the WEC design with high-effort approaches (large scale model testing and prototype testing at sea) afterwards to increase TRL.

### 1.1. Design and modeling of wave farms

In the context of wave farms, numerical and experimental studies focus on the interactions between the single WECs, which may be of hydrodynamic and/or mechanical nature (inter-farm moorings, power take-off (PTO) interactions, etc.). In the following, an extensive review of the relevant literature is presented. A focus is laid on the modeling of PTO systems. The PTO is the component of the WEC which converts the kinetic energy of the PA to electric energy. In prototypes, various PTO approaches are possible, e.g., hydraulic PTOs, direct mechanical drive systems, and direct electric drive systems (Pecher and Kofoed, 2017). In numerical models, the PTO is often reduced to a spring–damper system resembling a reactive controller, or a damper system resembling a passive controller.

Babarit (2013) provided a review of early investigations on WEC farms concluding that Boundary Element Method (BEM) codes were the only valid option for an appropriate analysis of wave farms. Compared to analytical models or Boussinesq/spectral models, BEM models can reproduce the hydrodynamics of complex oscillating structures accurately. Furthermore, mainly small wave farms with small WECs (PAs) were investigated then, for which the farm effects were deemed negligible. Data on larger wave farms or wave farms with larger devices were scarce due to the large computational resources needed for such investigations. However, negative farm effects were present, which increased with an increasing number of rows in the wave farm.

Further early and extensive investigations on WEC interaction in large wave farms were the experimental and numerical studies in the WECWakes project (Stratigaki et al., 2014a). Physical model tests with up to 25 heaving PAs were conducted. Based on the experimental results, intra- and extra-farm effects (effects in a farm respectively outside of a farm) were discussed. No clear statement on intra-farm effects could be made since positive and negative interactions were reported, which depend on farm layout and sea state. Nonetheless, the extra-farm effects were significant and could lead to a maximum wave damping of up to 20% behind the wave farm (Stratigaki et al., 2014a,b). Furthermore, the dissertation of Lamont-Kane (2015) summarizes numerical modeling approaches on wave farms.

Due to the aforementioned necessity to arrange WECs in wave farms, one major group of wave farm research activities investigates the optimal positioning of WECs in farms. Bozzi et al. (2017) studied the wave farm layout optimization using realistic wave data from different positions along the Italian shore in combination with simulations of different wave farm layouts. In this study, three distinct farm layouts (linear, square, rhombus) were compared using different PA separation distances and wave directions. BEM model inputs were used for the hydrodynamic simulations. Contrary to this study with a pre-defined set of wave farm layouts, the rise of machine learning (ML) optimization algorithms like Genetic Algorithms (GA), Particle Swarm Optimization (PSO), and similar approaches led to more general investigations without the pre-definition of farm layout. In recent years, these investigations have become dominant.

A typical example for most of the ML studies is presented by Zeng et al. (2022), who employ a potential flow-based radiation–diffraction solver for hydrodynamic calculations and use a GA to optimize the layout of a wave farm. In this case, the geometry of the WECs is simplified to a truncated regular cylinder, and a semi-analytical hydrodynamic model is used with a damper-only PTO. Hence, the hydrodynamic simulations have a short runtime, while a focus is put on the development of the GA to optimize the wave farm layout. In other studies, a BEM model (Ansys AQWA) is coupled with Matlab and the Ansys Parametric Design Language (APDL) to a Matlab-APDL-AQWA (MAA) simulation system. This system is used in combination with several optimization methods to assess their capabilities. A single PA and a two PA wave farm were studied. The design parameters are the PTO damping, the PA draft, and the spacing of the WECs (Cao et al., 2022). The MAA framework was further verified and used in a parametrical investigation on wave farms with up to ten WECs (Han et al., 2023a). Furthermore, the framework is also used in a study on farm optimization based on the farm wave field without using ML techniques (Han et al., 2023b). A similar APDL-Matlab-AQWA (AMA) system is proposed by Zhu et al. (2022), who validate the system based on experimental tests (Gong et al., 2022) of a three WEC wave farm. Furthermore, an Artificial Neural Network (ANN) is used to optimize farm layouts in combination with the AMA system for farms of up to eight devices. The runtime of the power calculation for one realization of a seven-device farm was 15 min using the AMA framework, indicating the long simulation times needed for optimization using this method. All four studies using the MAA/AMA framework and the respective experimental study employ passive control, i.e., the PTO consists of a damper.

A more thorough overview of wave farm optimization studies can be found in the reviews by Teixeira-Duarte et al. (2022) and Yang et al. (2022). Many of these optimization studies use a mid-fidelity hydrodynamic solver due to computational constraints, neglecting certain nonlinearities and viscosity. Since the farm layout is optimized for the operational state of the device, the disregard of the aforementioned effects is feasible. Nonetheless, the use of the mid-fidelity hydrodynamic solvers should be verified and validated. In the absence of model test data of the real device, open-source datasets are available for this purpose of verification and validation, but also for training of ML models. Recently, the SWELL (Standardised Wave Energy converter array Learning Library) dataset was published (Faedo et al., 2023), an experimental dataset of wave farms with up to five PA devices in nine different layouts. Different PTO mechanisms are modeled, i.e., a damper-only system and a spring–damper system.

To date, very few studies focus on wave farm modeling using high-fidelity CFD approaches: E.g., the modeling of a mechanically coupled wave farm employing a CFD solver coupled with a multibody dynamics solver is presented by Li et al. (2022), and Devolder et al. (2018) modeled farms of up to nine heaving PA devices, validating the results with data from the WECwakes project (Stratigaki et al., 2014a).

WEC-Sim is a mid-fidelity model commonly used for WEC design and modeling. In the following, studies on the application of WEC-Sim, with a focus on wave farms, are summarized. A general overview of the WEC-Sim applications by its developers and its users is given by Ogden et al. (2022). Wave farms were investigated in four studies. Balitsky et al. (2018) used WEC-Sim coupled with the BEM solver NEMOH to analyze the near-field hydrodynamic interactions within WEC farms. WEC-Sim was employed to model the PTO dynamics (hydraulic PTO system) in this study, while the wave fields (incident, radiated, diffracted) were modeled in NEMOH. In a further study, a similar group of authors added the wave propagation model MILDwave to the existing NEMOH-WEC-Sim model. The PTO is modeled as a linear damper. This three-model coupling approach allows a simulation of the intra-farm effects as well as the inter-farm effects (effects between single farms). The applicability of the model is shown by simulating ten farms of five oscillating surge WECs (OSWECs) on a sloping beach profile (Balitsky et al., 2019).

Similarly, Rollano et al. (2020) coupled WEC-Sim with two wave models, the phase-resolving wave model FUNWAVE-TVD and the phase-averaging model SWAN, aiming at studying the necessary input of the wave data for the modeled wave farms. They employed a one-way coupling approach, neglecting the interactions between the WECs due to their long separation distance, and concluded that the input data from a phase-resolving model is necessary to accurately calculate the potential power production of the wave farm. The PTO is represented as a linear damper.

Recently, Faraggiana et al. (2022) used WEC-Sim in combination with an optimizer (two nested GAs) to optimize wave farm layouts based on *Levelized Cost of Energy* (LCOE) minimization. The design parameters were the parameters of the linear PTO (stiffness, damping), the rated power of the wave farm, and the WEC spacing. While the former three parameters were optimized using an upper and lower limit of possible values, the WEC spacing was set to three discrete values, since the interactions of the single WECs had to be simulated by the BEM solver (NEMOH) before running the optimizer and WEC-Sim. This simplification again shows the current limitation of wave farm optimization due to limited computational resources, which leads to either strong simplifications in the hydrodynamic modeling, a limited design space in terms of device spacing, or the disregard of hydrodynamic interactions between the single devices. Each wave farm designer has to choose the most fitting simplification based on the properties of the respective WECs and wave farm at hand.

### 1.2. Objectives

While this paper does not aim at the optimization of a wave farm layout, it contributes to the solution of the problem pointed out at the end of Section 1.1 by validating WEC-Sim and discussing its accuracy based on the chosen simplifications and the necessary accuracy of input data. The simplification employed in this study is the disregard of the hydrodynamic interactions between the single PAs since the mechanical interactions are deemed dominant, as discussed in a prior experimental study (Meyer et al., 2023).

Concerning wave farms, several research questions regarding the conjunction of physical model testing and numerical simulations arise in the context of concept and design validation. This study aims to answer the following research questions:

- On the accuracy of different modeling approaches: Can first insights on wave farm performance be gained from mid-fidelity models, or is higher fidelity modeling necessary, e.g., physical model tests or high-fidelity simulations?
- On the necessary level of fidelity of the input data: Are BEM simulations sufficient as input for mid-fidelity models, or are higher fidelity simulations and/or experimental data indispensable?
- On wave farm effects (mechanical, hydrodynamic, and mooring interaction) in mechanically coupled wave farms: Which effects are of relevance, and which effects can be simplified or even neglected?

A wave farm with 24 PAs, rigidly connected via a frame superstructure, will be used as the study object. Its power output is assessed from simulations using the mid-fidelity hydrodynamic model WEC-Sim. The influence of three different calibration strategies on the accuracy of the hydrodynamic model is investigated: (i) a low-effort calibration, which solely uses the initial hydrodynamic results for the PAs and the initial mooring properties; (ii) a medium-effort approach, which uses calibrated BEM data based on physical model tests but still employs the initial mooring configuration; and (iii) a high-effort approach, which uses the calibrated BEM data and calibrated mooring settings based on a calibration with model test data of the wave farm (Meyer et al., 2023).

In the present study, additional model tests of a single PA will be analyzed. Afterwards, the results of both, the wave farm and single PA model test campaign, will be used to calibrate numerical simulations using WEC-Sim. Based on this, the aforementioned research questions will be discussed.

### 1.3. Outline

This paper is structured as follows: Following this introduction, the methodology of the model tests, the basic equations of the simulation models, and the calibration workflow are described in Section 2. Afterwards, the results of the physical model tests and the numerical simulations are presented and discussed in Section 3. Finally, a summary and a conclusion are presented in Section 4 before giving an outlook to future studies.

## 2. Methodology

### 2.1. Wave farm

The wave farm is a concept by *SinnPower GmbH*, which aims at reducing CAPEX and mooring costs by connecting individual PAs via a rigid frame superstructure (Sinn, 2016). The system is modular, such that the length and width of the farm as well as the number of PAs can be adapted to site-specific conditions. The previous experimental study (Meyer et al., 2023) investigated a wave farm comprising 24 PAs. All system parameters (geometry, PTO, etc.) refer to the aforementioned realistic wave farm concept. The 24 PAs were organized in four columns (parallel to the incident wave direction, distance = 0.41 m) and six rows (perpendicular to the incident wave direction, distance = 0.8 m). A PTO mechanism allows vertical relative motion between PA and superstructure. Due to experimental constraints, this PTO was represented using a linear spring with a spring constant of $k = 43\,\mathrm{N\,m^{-1}}$ in the model tests. No damper was applied.

**Remark.** The authors are aware that a mass–spring system cannot represent an actual PTO. However, experimental constraints, which are explained in Meyer et al. (2023), did not allow the arrangement of a damper. A damper is added in the subsequent numerical simulations for a realistic PTO representation.

A rendering of the wave farm is presented in Fig. 1. Each PA is allowed to move independently in the reference frame of the PTO. The force exerted from PA to PTO is subsequently exerted from PTO to the rigid superstructure. Hence, the wave farm moves differently depending on the incident wave conditions. In particular, the incident wavelength and its relation to the wave farm length influence the wave farm's motion response significantly. Fig. 2 presents two schematic drawings to emphasize this influence. Waves with an incident length that is larger than the array length lead to a large pitch response of the superstructure, as depicted in Fig. 2(a). Fig. 2(b) represents the wave farm response in waves with a wavelength shorter than the wave farm length. Here, an overall reduced motion response of the superstructure is expected. The latter conditions are deemed favorable since the relative motion between individual PAs and superstructure,

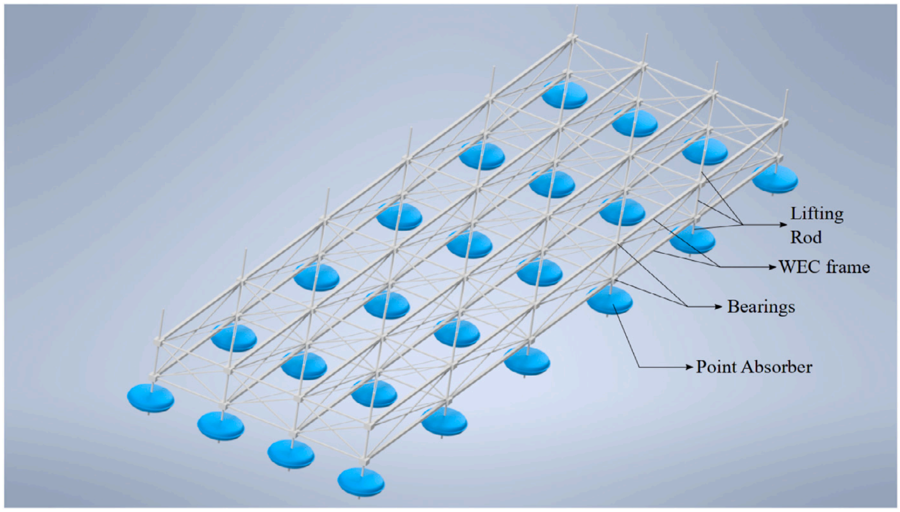


**Fig. 1.** Rendering of the wave farm.

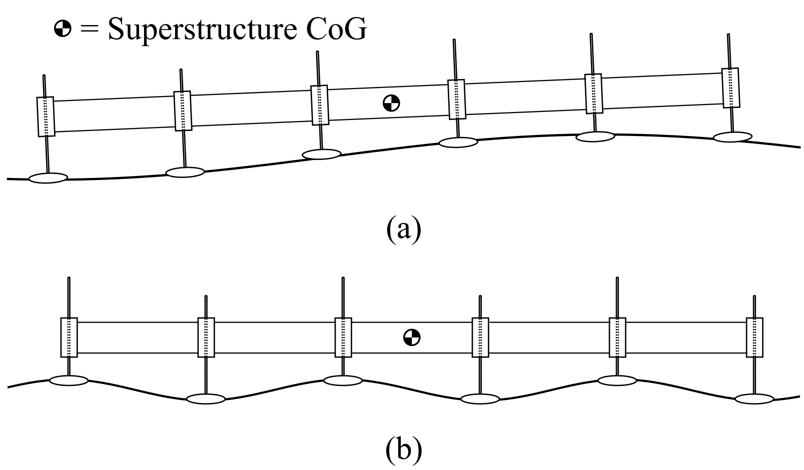


**Fig. 2.** Representation of relation between incident wavelength and WEC array motion: (a) Large incident wavelength, (b) Small incident wavelength.

which leads to the energy conversion, is largest with a nearly stationary superstructure. Furthermore, Fig. 2 indicates the position of the superstructure's center of gravity (CoG). The distance between PA and superstructure CoG directly influences the impact the individual PA motion has on the superstructure pitch motion: PAs in the first or last PA row have a large lever arm due to the large distance to the superstructure's CoG. Subsequently, the respective PTO force leads to a larger rotational moment than for PAs with less distance to the CoG.

### 2.2. Physical model tests: Wave farm

Two model test campaigns are used in the subsequent calibration of the numerical model. The first model test campaign was conducted using the whole wave farm, investigating the influence of different mooring systems on the motion and energy conversion potential (ECP) of the WEC. The ECP is used as an indirect measure of WEC efficiency by evaluating the relative velocity between each PA and the superstructure. This alternative evaluation methodology was necessary since realistic energy conversion could not be calculated due to the missing damper in the model test PTO. Hence, the relative velocity between the PAs and the superstructure was evaluated. The model test methodology and the respective results were published in Meyer et al. (2023). A detailed description of the model test setup and the data evaluation can be found there. For the sake of completeness, a summary is given in the following:

The physical model tests were conducted in the wave flume "Schneiderberg" (WKS, *German: Wellenkanal Schneiderberg*) on a scale of 1/15. The flume has a length of 110 m and a width of 2.2 m. The water depth was set to 1 m. A piston-type wavemaker was used for wave generation, while a stepped revetment ensured passive wave absorption at the opposite end of the flume. The wave farm was subject to regular waves with three heights (0.08 m–0.2 m) and 16 wave periods (1.0 s–2.5 s).

Four different mooring approaches were investigated: A free-floating reference case, a taut mooring, a catenary mooring, and a vertical tension leg-type mooring. The motion response of the superstructure and each PA was measured using a motion tracking system. The relative motion of PAs and superstructure was used to calculate the ECP. Based on the ECP, the mooring systems were evaluated. The overall motion response of the wave farm was divided into three wavelength ranges:

- Short wavelength range ($L < 0.8 \cdot L_{Farm}$): high ECP; small motion response of superstructure; small mooring influence on ECP
- Medium wavelength range ($0.8 \cdot L_{Farm} \leq L \leq 1.25 \cdot L_{Farm}$): decreasing ECP; increasing motion response of superstructure; taut mooring system leads to highest ECP
- Long wavelength range ($L > 1.25 \cdot L_{Farm}$): Small ECP; large motion response of superstructure; vertical tension leg-type system leads to highest ECP

Due to the overall reduced ECP in the long wavelength regime, the taut mooring system was deemed the best initial design choice.

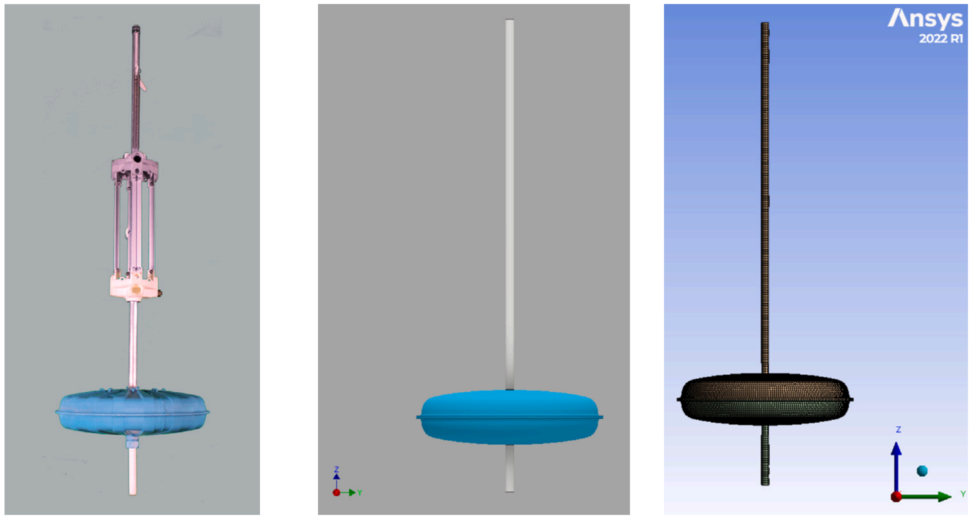


(a) (b) (c)

**Fig. 3.** Detail view of a single point absorber: (a) Physical structure, (b) CAD representation for numerical modeling, (c) Mesh used in Ansys AQWA simulations.

### *2.3. Physical model tests: Point absorber*

A second campaign focusing on a single PA was also conducted in the wave flume "Schneiderberg" with a water depth of 0.75 m. The difference in water depth between the two model test campaigns is discussed in Section 3.

#### *2.3.1. Test setup*

One PA was extracted from the wave farm model, including its static frame, i.e., the bearing and the attachment point of the spring PTO. Fig. 3(a) depicts a side view of the PA. Furthermore, the respective CAD model used for the numerical simulations is presented in Fig. 3(b) and the mesh used in the numerical simulations is displayed in Fig. 3(c). The PA has a diameter $D$ of 0.23 m. A schematic drawing of the test setup is shown in Figs. 4 (a) and (b). The static frame was connected rigidly to the flume walls using aluminum profiles. Its vertical position was equal to the equilibrium position of the wave farm setup. This exact positioning is of high importance since it directly affects the pretension of the PTO spring, which also controls the draft of the PA. The PTO allows heave motion while restricting every other degree of freedom. A six-axis force/torque transducer (*ATI FT-Gamma SI-65-5*) was placed at the attachment point of the PA's static part and the aluminum profiles to measure the forces exerted onto the PA model.

The wave elevation was measured using ultrasonic wave gauges (*General Acoustics Ultralab ULS*). Seven wave gauges were used in total. Wave gauge 1 was placed at a distance of 1.90 m from the PA to measure the undisturbed incident wave height, while six wave gauges were placed close to the PA to measure wave reflection, radiation, and transmission (see Fig. 4(b)). Wave gauge 2 was placed at 1D (measured from the PA center) in front of the PA to allow the investigation of wave reflection. Four wave gauges (4–7) were placed at 1D - 4D behind the PA to measure wave transmission. Furthermore, wave gauge 3 was placed at 1D next to the PA to enable an evaluation of wave radiation and diffraction. A *Qualisys* motion tracking system was used to measure the heave motion of the PA. One passive (reflective) marker was attached to the top of the PA's lifting rod. Fig. 5 shows a picture of the test setup in the wave flume, while Table 1 summarizes the measurement equipment.

#### *2.3.2. Test matrix*

Two setups were investigated in the model test campaign: Freely floating (no PTO) and spring PTO (spring stiffness $c = 43\,\mathrm{N\,m^{-1}}$). The spring PTO was used in the wave farm model test campaign.

**Table 1**
Measurement equipment.

| Sensor | Manufacturer | Name |
|---|---|---|
| Force/Torque Transducer | ATI | FT-Gamma SI-65-5 |
| Motion Tracking System | Qualisys | 6+ (four cameras) |
| Wave measurement system | General Acoustics | Ultralab ULS |

**Table 2**
Test matrix of regular wave conditions for the single PA model tests.

| Wave period [s] | | Wave height [m] | |
|---|---|---|---|
| Scaled | Prototype | Scaled | Prototype |
| 1.0 | 3.87 | 0.08 | 1.2 |
| 1.2 | 4.65 | 0.08 | 1.2 |
| 1.4 | 5.42 | 0.08 | 1.2 |
| 1.6 | 6.20 | 0.08 | 1.2 |
| 1.8 | 6.97 | 0.08 | 1.2 |
| 2.0 | 7.75 | 0.08 | 1.2 |
| 2.2 | 8.52 | 0.08 | 1.2 |
| 2.4 | 9.30 | 0.08 | 1.2 |
| 2.6 | 10.06 | 0.08 | 1.2 |
| 2.8 | 10.84 | 0.08 | 1.2 |
| 3.0 | 11.62 | 0.08 | 1.2 |

Regular wave conditions with one wave height and eleven different wave periods were used. The wave height was chosen in accordance with the lowest wave height tested in the wave farm model tests. Since the purpose of the model test was the calibration of a linear model, only the smallest wave height was used.

In addition to the regular wave test cases with PA, all test cases were repeated without the PA to gather information on the undisturbed wave field. Table 2 summarizes the regular wave test conditions.

#### *2.3.3. Data evaluation*

The analysis and discussion of the model test results focus on two main quantities: The heave motion and the surge force. Both quantities are evaluated in the frequency domain using *Fast Fourier Transform* (FFT). An interrogation window is used to define the input for the FFT. This interrogation window comprises the steady-state oscillations of heave motion and wave force, omitting wave reflections and the initial transient phase of the oscillation. Hence, the first five waves after reaching the full wave height are omitted before the start of the interrogation window. To avoid the influence of reflected waves, the

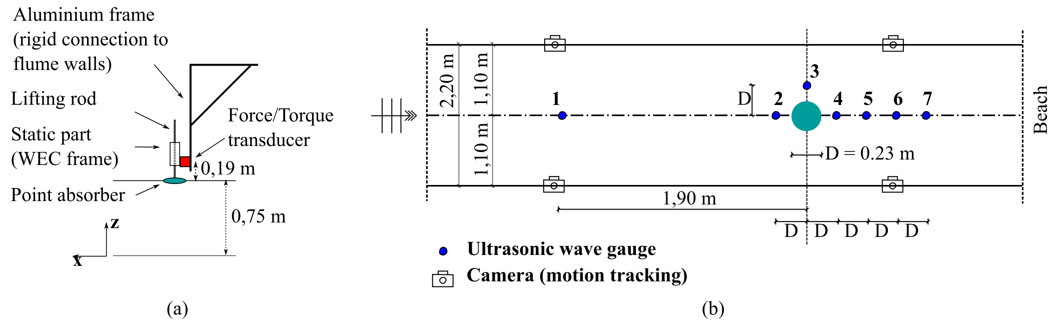


**Fig. 4.** Model test setup: (a) Side view, (b) Top view.

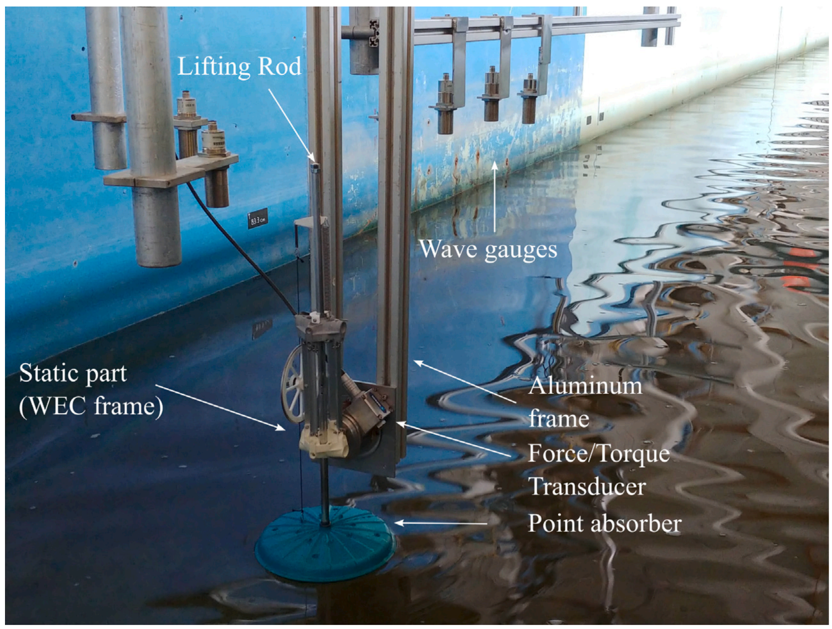


**Fig. 5.** Photo of the model test setup.

interrogation window has a length of four complete wave periods. Fig. 6 shows an example of the measured time series of wave elevation, heave motion, and surge force as well as the interrogation window and the subsequent amplitude spectra.

The heave motion is summarized using the response amplitude operator (RAO), which is a measure of motion response amplitude and wave amplitude.

$$\text{RAO:} \qquad \frac{a_z}{a_\zeta}, \tag{1}$$

with the heave amplitude at wave frequency $a_z$ and the incident wave amplitude $a_\zeta$.

A similar approach is used to evaluate the surge force, calculating a force amplitude ratio (FAR):

$$\text{FAR:} \qquad \frac{a_{F_x}}{a_\zeta}, \tag{2}$$

with the surge force amplitude at wave frequency $a_{F_x}$.

The incident wave amplitude is calculated using the undisturbed wave field recorded in the test setup without PA. These zero-tests were synchronized with the PA tests using the cross-correlation between the wave gauges in the respective tests.

### 2.4. Numerical modeling

All numerical simulations are conducted on a model scale (1/15). The numerical simulations presented in this paper are performed using WEC-Sim v5.0.1 (Ruehl et al., 2022), which is coupled with the mooring model MoorDyn v1.01.02 (Hall, 2021). WEC-Sim requires frequency-dependent input data of wave excitation force as well as added mass and damping (radiation force). This input data is usually generated using BEM simulations, but it can also be user-generated based on data from high-fidelity numerical simulations or physical modeling (NREL & Sandia, 2023). In the present study, Ansys AQWA in version 2022 R1 (ANSYS, 2022) is employed for BEM simulations.

In the following, the basic principles and governing equations of the three simulation models WEC-Sim, MoorDyn, and Ansys AQWA are summarized.

#### 2.4.1. WEC-Sim

WEC-Sim is a multibody simulation model for the modeling and design of WECs. It solves the equation of motion in the time domain:

$$m\ddot{X} = F_{exc}(t) + F_{rad}(t) + F_{PTO}(t) + F_B(t) + F_m(t), \tag{3}$$

with the structural mass $m$, the acceleration vector $\ddot{X}$, the wave excitation force $F_{exc}(t)$, the radiation force $F_{rad}(t)$, the PTO force $F_{PTO}(t)$,

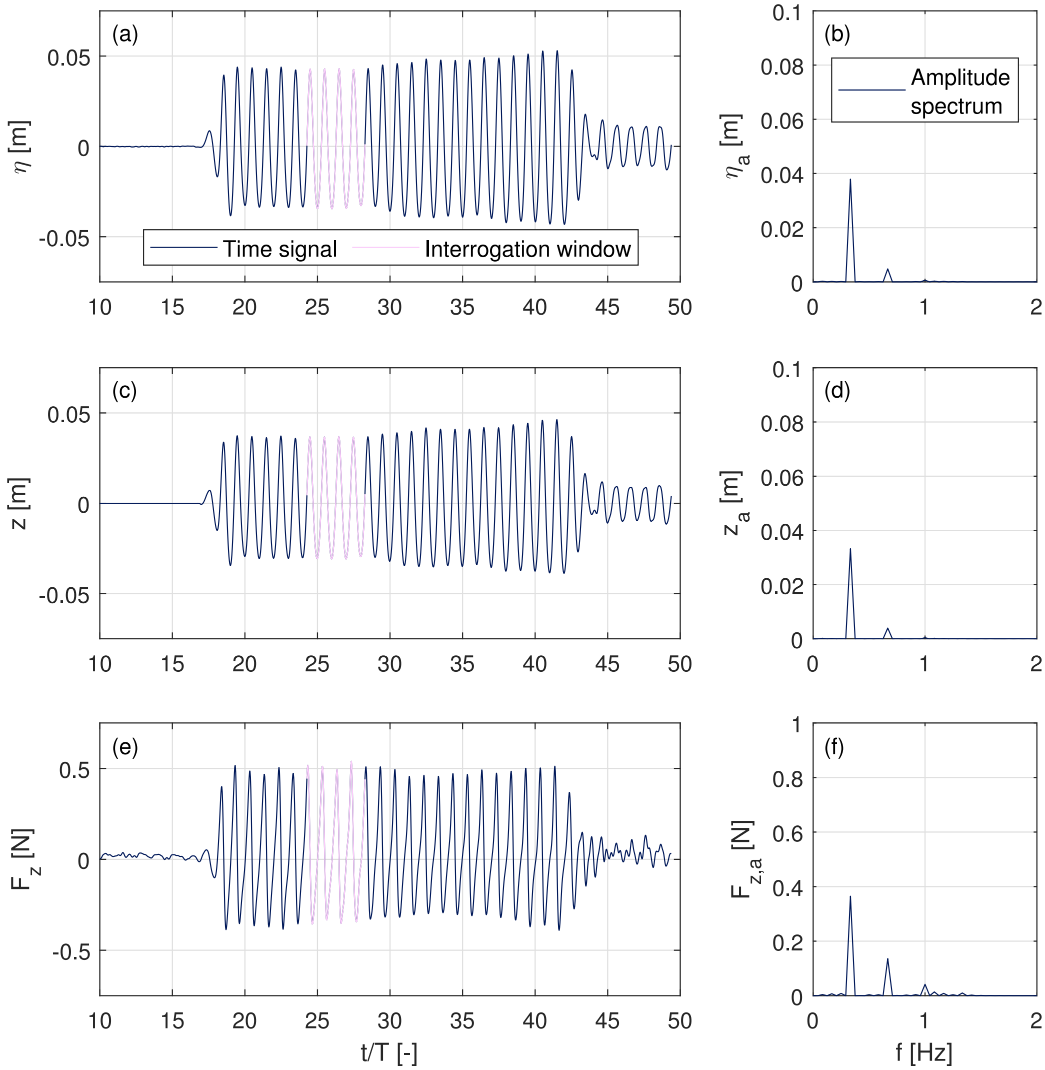


**Fig. 6.** Definition of interrogation window and subsequent FFT results: (a) Wave time series, (b) Wave amplitude spectrum, (c) Heave time series, (d) Heave amplitude spectrum, (e) Surge force time series, (f) Surge force amplitude spectrum.

the net buoyancy force $F_B(t)$, and the mooring force $F_m(t)$. Additional forces, e.g., viscous forces from Morison elements, can be incorporated. Since they are not used in the present study, such forces are not shown in Eq. (3).

The excitation, radiation, and buoyancy force depend on the hydrodynamic coefficients obtained in the BEM simulations. In the present study, Ansys AQWA is as the BEM simulation model. Its governing equations are summarized in Section 2.4.2. Different options are available for the calculation of the aforementioned forces:

The excitation force comprises a Froude–Krylov term, which incorporates the pressure field from the undisturbed wave, and a diffraction term, which incorporates the wave diffraction due to the structure. In the linear approach, which is mainly used in this study, the Froude–Krylov term and the diffraction term are added to form the wave excitation force complex amplitude $F_{exc}(\omega, \Theta)$, which depends on the incident wave frequency $\omega$ and the incident wave direction $\Theta$. In regular waves, the wave excitation force $F_{exc,r}(t)$ is calculated as follows:

$$F_{exc,r}(t) = \Re\left[\frac{H}{2} F_{exc}(\omega, \Theta) e^{i\omega t}\right], \tag{4}$$

with $\Re$ indicating the real part of the term in square brackets, and the incident wave height $H$.

Irregular wave spectra are represented in the time domain as a linear superposition of regular waves. Hence, the following term is used to calculate the wave excitation force $F_{exc,irr}(t)$:

$$F_{exc,irr}(t) = \Re\left[\sum_{j=1}^{N} F_{exc}(\omega_j, \Theta) e^{i\omega_j t + \varphi_j} \sqrt{2S(\omega_j) d\omega_j}\right], \tag{5}$$

with the number of frequency bands $N$, the random phase angle $\varphi$, and the frequency-dependent wave energy distribution $S(\omega)$.

The radiation force can be calculated using two different approaches: One steady-state approach $F_{rad,ss}(t)$, which is valid in regular waves, and a more general approach $F_{rad,c}(t)$ using Cummins equation (Cummins, 1962), which is valid in regular and irregular waves.

$$F_{rad,ss}(t) = -A(\omega)\ddot{X} - B(\omega)\dot{X} \tag{6}$$

In Eq. (6), $A$ is the frequency-dependent added mass matrix, $B$ is the frequency-dependent radiation damping matrix, and $\dot{X}$ is the velocity vector.

$$F_{rad,c}(t) = -A_\infty \ddot{X} - \int_0^t K_r(t-\tau)\dot{X}(\tau)d\tau \tag{7}$$

In Eq. (7), $A_\infty$ is the added mass matrix at infinite frequency and $K_r$ is the radiation impulse response function:

$$K_r = \frac{2}{\pi}\int_0^\infty B(\omega)cos(\omega t)d\omega \tag{8}$$

The calculation of $F_{rad,c}$ using a convolution integral is a time-consuming approach. In this paper, the state-space representation of this integral is used for the simulation of irregular sea states to reduce computational time. The steady-state form is already implemented in WEC-Sim, which reduces the partial differential equation needed to calculate $K_r$ to a linear system. Further information on the theoretical background of this implementation can be found in the WEC-Sim documentation (NREL & Sandia, 2023) and, with further detail, in Kung (1978), Kristiansen et al. (2005), Taghipour et al. (2008).

In addition to the previously presented linear approaches, a weakly nonlinear approach is implemented as well. In that case, Froude–Krylov and buoyancy force can be calculated using the instantaneous wave profile and the body displacement. Therefore, the structure's topology has to be provided using a stereolithography (STL) file.

The net buoyancy force comprises gravity force and buoyancy force, depending on the structure's mass, its hydrostatic stiffness $K_h$ (derived from geometry or the BEM model), and its displacement.

The PTO force $F_{PTO}$ is calculated following

$$F_{PTO}(t) = -K_{PTO} X_r(t) - C_{PTO} \dot{X}_r(t), \tag{9}$$

with the PTO stiffness $K_{PTO}$, the PTO damping $C_{PTO}$, the relative position $X_r$, and the relative velocity $\dot{X}_r$. In this context, the term "relative" denotes the relation between the PTO base (e.g., fixed structure or wave farm superstructure) and the PTO follower (i.e., PA).

The PTO force can be separated into a reactive force component (first part of Eq. (9)) and a resistive force component (second part of Eq. (9)). Based on this PTO force, the PTO power $P_{PTO}(t)$ can be obtained:

$$P_{PTO}(t) = F_{PTO}(t)\dot{X}_r(t) \tag{10}$$

Only the resistive component of the PTO force influences the time average of the PTO power $P_{PTO}$ since the time average of the reactive force component is zero (Pecher and Kofoed, 2017).

The mooring force $F_m(t)$ can be calculated using two options: A linear mooring matrix or via the external lumped-mass mooring model MoorDyn. Both approaches are used in the scope of this paper. The linear mooring matrix resembles a spring–damper system. Hence, the mooring force $F_m(t)$ is calculated as follows:

$$F_m(t) = B_m \cdot \dot{X}(t) + C_m \cdot X(t), \tag{11}$$

with the mooring damping matrix $B_m$, the mooring stiffness matrix $C_m$, the velocity vector $\dot{X}(t)$, and the position vector $X(t)$.
Furthermore, the position of the mooring system as well as its pretension needs to be defined.

Compared to the linear mooring matrix, MoorDyn uses a more complex approach to model the mooring influence. This approach is a lumped-mass implementation, separating each mooring line into segments of equal length. The number of segments $S$ can be set by the user. Furthermore, $S + 1$ nodes are created at the connection points between the segments. The physical properties (e.g., diameter, unstretched length) of each segment can be defined by the user. The model calculates the acceleration of each node using internal forces (i.e., axial stiffness and damping), weight force (including buoyancy), and hydrodynamic forces (added mass and drag from the Morison equation). Furthermore, a seabed contact force can be respected, which is not relevant for the present study since a taut mooring system is simulated. Further information on the calculation of internal forces and hydromechanical forces can be found in a publication by Hall and Goupee (2015). The coupling between MoorDyn and WEC-Sim was validated by Sirnivas et al. (2016). Furthermore, MoorDyn is coupled to many other Open-Source models, e.g., OpenFAST (Hall and Goupee, 2015) or DualSPHysics (Domínguez et al., 2019). It is important to note that the current implementation of the coupling between MoorDyn and WEC-Sim disregards wave forces on the mooring lines, while other hydrodynamic (i.e., drag and inertia from Morison equation due to motion relative to still water) and hydrostatic forces (i.e., buoyancy) are considered in the simulations.

### 2.4.2. Ansys AQWA

Ansys AQWA is a simulation model that is used to derive the hydrodynamic coefficients using linear potential flow theory, assuming an incompressible and irrotational fluid, together with small amplitudes of the incident wave and respective motion response of the structure. Hence, viscous effects are neglected and a velocity potential $\phi$ can be defined:

$$v = \nabla\phi, \tag{12}$$

with the fluid velocity vector $v$ and the operator $\nabla$.

The divergence of the velocity is equal to 0 (Laplace equation):

$$\nabla \cdot v = \nabla^2\phi = 0. \tag{13}$$

The velocity potential can be split further into an incident wave potential $\phi_0$, a radiation potential $\phi_r$, and a diffraction potential $\phi_d$:

$$\phi = \phi_0 + \phi_r + \phi_d. \tag{14}$$

These three potentials can be solved to calculate the hydrodynamic coefficients (i.e., added mass $A$, wave radiation damping $B$, Froude–Krylov excitation force $F_{exc,FK}$, and diffraction excitation force $F_{exc,dfr}$) using Green's function by distributing boundary elements or panels over the wetted body surface. A more detailed overview of the theoretical background, boundary conditions, and the applications of BEM models in wave energy is given by Papillon et al. (2020).

In addition to the frequency-domain modeling approach, Ansys AQWA can also obtain results in the time domain. Since this time domain model is based on the same foundations as WEC-Sim, its details will be shortly summarized in Section 2.4.4.

### 2.4.3. Data evaluation

The data evaluation of the numerical simulations uses the same principles applied in the evaluation of the experimental data explained in Section 2.3.3. I.e., FFT analyses of motion, force, and wave elevation time series.

However, the interrogation window is defined differently due to the absence of wave reflection in the numerical models. A fixed number of five full oscillation cycles before the end of the simulation is evaluated in regular wave simulations. For both, single PA and wave farm simulations, the runtime was 50 s.

Following the single PA model tests, heave response and surge force are evaluated in the single PA simulations.

In the wave farm simulations, the following quantities are evaluated:

- Surge response $a_{x,F}$ and surge RAO
- Heave response $a_{z,F}$ and heave RAO
- Pitch response $a_{\Theta,F}$ and pitch RAO
- Only for simulations in sea states: Absorbed Power $P$ for each PA

The wave farm responses are evaluated at the COG of the superstructure as depicted in Fig. 2.

### 2.4.4. Numerical setup & calibration methodology

In the following, the set of WEC-Sim simulations and the subsequent calibrations conducted in this study are explained. The simulation workflow is presented in Fig. 7.

At first, the BEM data is generated in the frequency domain using Ansys AQWA. Afterwards, this BEM data is used in WEC-Sim time-domain simulations. As mentioned at the end of Section 2.4.2, Ansys AQWA can obtain time domain results based on the frequency domain BEM results as well. Ansys AQWA uses a similar approach to the convolution integral formulation for the nonlinear calculation of the Froude–Krylov force and the nonlinear calculation of the buoyancy force. In Section 3, firstly the time domain modeling of Ansys AQWA and WEC-Sim are compared. Here, different settings concerning the nonlinearity of the simulations are used, which are summarized in Table 3.

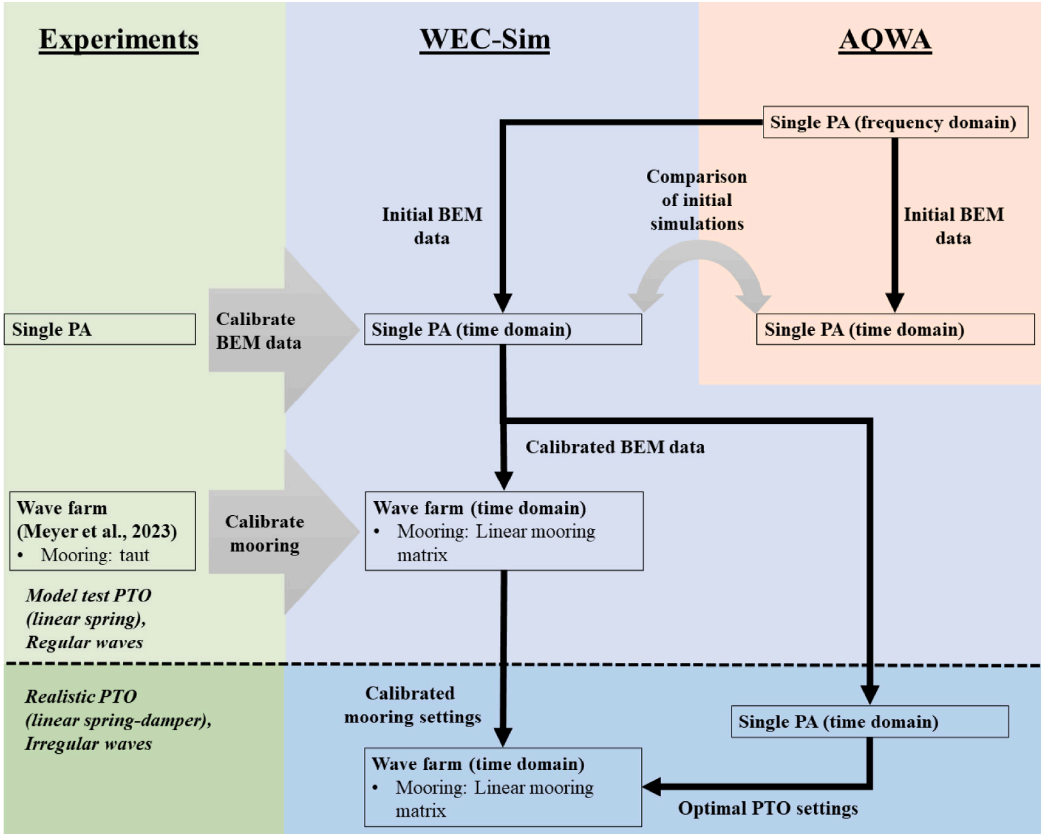


**Fig. 7.** Workflow of the study.

**Table 3**
Overview of the simulation approaches used in this study.

| Name | Analysis type | | Linearity assumptions | |
|---|---|---|---|---|
| | FD | TD | $F_{FK}(t)$ | $F_B(t)$ |
| AQWA | x | | Linear | Linear |
| WEC-Sim, linear | | x | Linear | Linear |
| WEC-Sim, nonlinear | | x | Nonlinear | Nonlinear |
| AQWA, Time response, nonlinear | | x | Nonlinear | Nonlinear |
| AQWA, Time response, linear | | x | Nonlinear | Linear |
| AQWA, Time response (FA) | | x | Linear | Linear |

**Remark.** At this point, the difference between Ansys AQWA and WEC-Sim should be clarified: Ansys AQWA is a model focusing on hydrodynamic calculations, while WEC-Sim focuses on the multi-body interactions of WECs. Ansys AQWA's time-domain simulations are limited regarding body-to-body interactions, i.e., PTOs or constraints. Hence, the large wave farm used in this study cannot be simulated completely in Ansys AQWA. Furthermore, the mesh size in Ansys AQWA is limited to 40,000 elements (in the utilized academic version). Therefore, the simultaneous simulation of an array of 24 PAs would require a coarse mesh for each PA. Using WEC-Sim, these limitations of Ansys AQWA can be overcome to simulate the complete wave farm. On the one hand, the BEM results were obtained for only one single PA and then copied to use them for all 24 PAs. Of course, this approach neglects the interaction of the PAs. On the other hand, WEC-Sim allows for a large number of PTOs and constraints due to its coupling with *Matlab/Simulink* and the multi-body dynamics model *Simscape Multibody*.

To calibrate the BEM data, WEC-Sim simulations of the single PA in regular waves are conducted and the results are compared with the experimental data. Based on this comparison, the calibration of the WEC-Sim input data is achieved by artificially adapting the amplitude of the wave excitation force complex amplitude $F_{exc}(\omega,\Theta)$. An error measure $\varepsilon$ is defined to quantify the difference between simulations and experiments.

$$\varepsilon = \frac{x_{num,i}}{x_{exp,i}} - 1\,, \tag{15}$$

with the experimental value $x_{exp,i}$ and the simulated value $x_{num,i}$ for regular wave condition $i$. Using Eq. (15), a negative $\varepsilon$ denotes an underestimation of the experimental values in the simulation, while a positive $\varepsilon$ denotes an overestimation.

Subsequently, the wave farm is simulated in regular waves, and the respective results of the superstructure's motions (i.e., surge, heave, and pitch response) are compared with the experimental data from Meyer et al. (2023). While in the previous publication, three mooring systems were compared only the taut mooring system is used in the present simulations. Fig. 8 shows a schematic drawing of the mooring system. The calibration of the wave farm simulations is achieved by adapting the mooring settings, such that the motion response of the wave farm matches the experimental data with the least error. Therefore, the *normalized root mean square error* (nRMSE) is used as an evaluation value, while achieving normalization using the range (from minimum to maximum) of experimental data:

$$\text{nRMSE:} \quad \sqrt{\sum_{i=1}^{N} \frac{\left(x_{exp,i} - x_{num,i}\right)^2}{N}} / (x_{exp,max} - x_{exp,min})\,, \tag{16}$$

with the number of regular wave conditions $N$.

The simulation settings for both single PA and wave farm simulations are summarized in Table 4.

For the calibrations, the model test PTO (linear spring, no damper) was used. After finalizing both calibrations, the power output of the wave farm in different irregular sea states is compared for all three

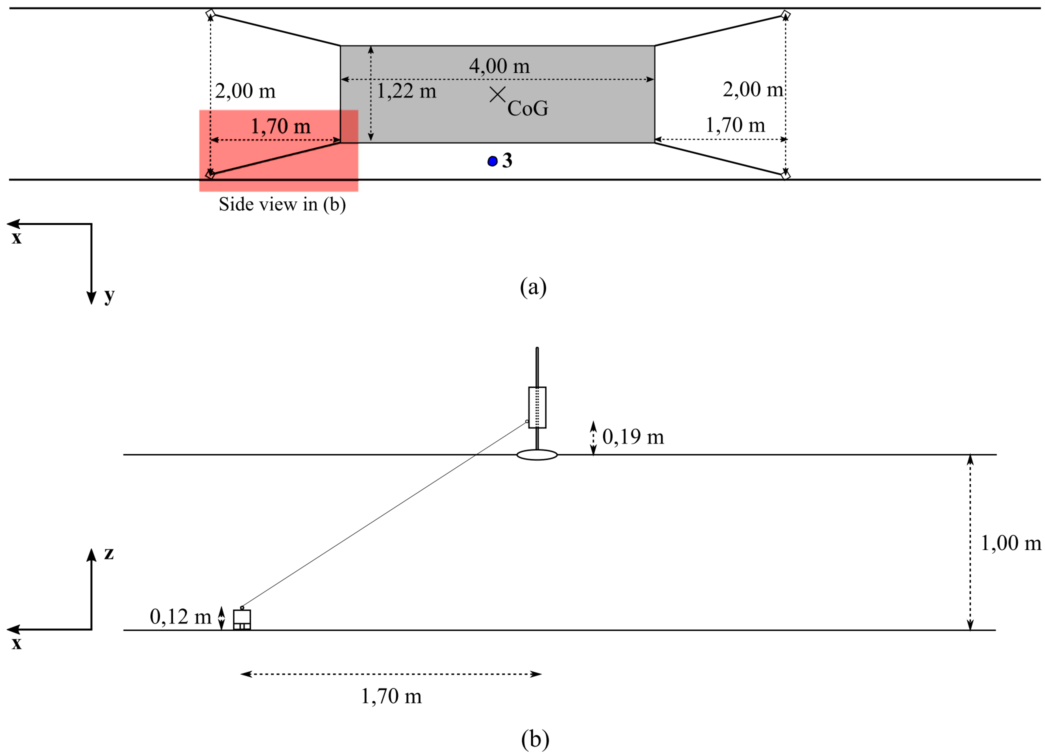


**Fig. 8.** Schematic drawing of the taut mooring system: (a) Top view, (b) Side view of a single mooring line).

**Table 4**
Summary of simulation settings: Wave farm, PTO, mooring, simulation settings (PTO settings are only valid for calibration and are altered in the simulations for power assessment).

| Parameter | Value | | Unit |
|---|---|---|---|
| | Scaled | Prototype | |
| $m_{PA}$ | 0.47 | 1586 | kg |
| $dx_{PA}$ | 0.8 | 12 | m |
| $dy_{PA}$ | 0.41 | 6.15 | m |
| $m_{Frame}$ | 13.08 | 44 145 | kg |
| $I_{xx,Frame}$ | 2.73 | 2.0883 e+06 | kg m$^2$ |
| $I_{yy,Frame}$ | 22.62 | 17.177 e+06 | kg m$^2$ |
| $I_{zz,Frame}$ | 25.01 | 18.992 e+06 | kg m$^2$ |
| $K_{PTO}$ | 43 | 9675 | N/m |
| $C_{PTO}$ | 0 | 0 | N/(m/s) |
| PTO Pretension | 0.00584 | 19.7 | kN |
| $m_{Mooring,dry}$ | 0.04 | 9 | kg/m |
| $EA_{Mooring}$ | 0.485 | 1636.875 | kN |
| $L_{0,Mooring}$ | 2.022 | 30.33 | m |
| Dist. Anchor - Fairlead | 2.044 | 30.66 | m |
| Timestepping | 4th order Runge Kutta | | |
| dt (regular waves) | 0.005 (constant) | | s |
| dt (irregular waves) | 0.002 (constant) | | s |

approaches: no calibration, single PA calibration, and wave farm calibration. Therefore, a realistic PTO is employed and a reactive controller (proportional-integral controller, PI controller) is implemented in Simulink. The Simulink diagrams of a solo single PA, the wave farm, a single PA in the wave farm, and the reactive controller are displayed Appendix B, Fig. B.19.

The optimal PTO settings are found using simulations of the solo single PA, similar to the approach in Penalba et al. (2018). Han et al. (2023b) showed that the optimum PTO configurations for wave farms can be derived from single-device optimization. Finally, the difference in the power output based on the three calibration approaches is assessed.

The approach of this study is to use BEM simulations of one single PA as an input for all PAs for the wave farm simulations. To achieve this, the data of the single PA needs to be adapted. On the one hand, its x- and y-position need to be changed accordingly. On the other hand, the phase information of the wave excitation force needs to be adapted. Without this phase adaptation, all PAs move in phase with the wave at the coordinate origin, neglecting their respective position, since WEC-Sim uses the wave elevation at the coordinate system's origin to calculate the wave excitation force $F_{exc}(t)$.

The phase adaptation $dp$ was achieved based on linear wave theory, using the celerity of the linear waves $c$:

$$c = L/T \tag{17}$$

$$dr = \sqrt{(dx\cos(\Theta))^2 + (dy\sin(\Theta))^2} \tag{18}$$

$$dw = \frac{dr}{c} \tag{19}$$

$$dp = \omega \cdot dw \tag{20}$$

with the incident wave length $L$, the incident wave period $T$, the distance from PA to origin $dr$, the x- and y- coordinate of this distance $dx$ and $dy$, and the corresponding wave delay $dw$.

The phase adaptation $dp$ was calculated for each PA in the wave farm. Subsequently, the phase of the incident wave force was adapted by adding $dp$ to the phase information from the BEM simulations of the single PA. The present approach neglects hydrodynamic interactions between the individual point absorbers, since only one single PA is implemented in the BEM simulations. Accordingly, Eq. (20) assumes that the incident wave elevation is the same for each point absorber, neglecting any wave height reduction due to the upstream PAs. However, only this adaptation enables WEC-Sim simulations of the wave farm with individual, position-dependent PA response in WEC-Sim using BEM input data from Ansys AQWA.

## 3. Results and discussion

In the following, the results of the study are presented and discussed. All results are given in prototype scale. After analyzing the

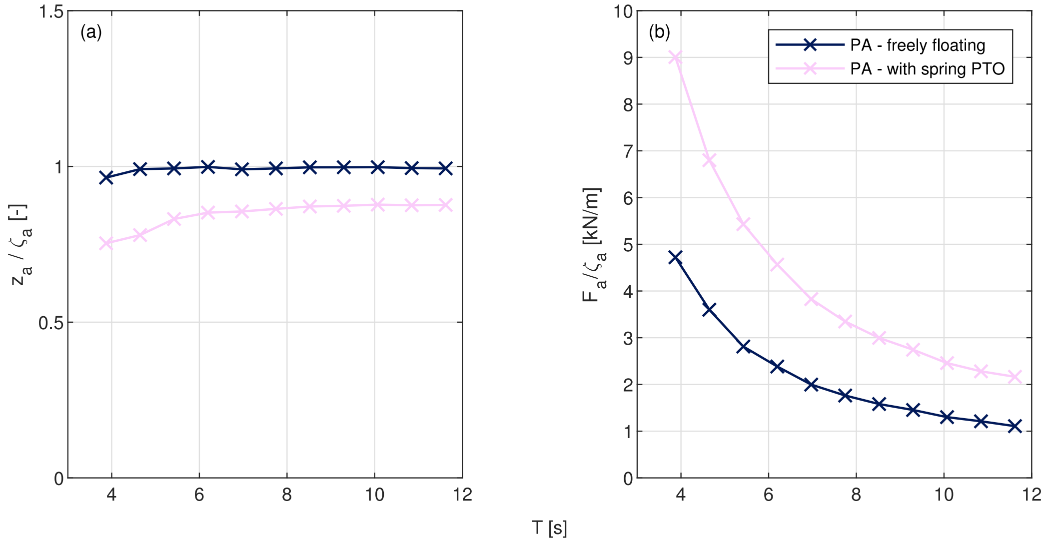


**Fig. 9.** Model test results for one single PA: (a) Heave response, (b) Surge force.

experimental results of the single PA model tests, the subsequent numerical simulations of the single PA are presented. Afterwards, the wave farm simulations are discussed in conjunction with the different calibration approaches, focusing on the estimated energy output of the wave farm.

### 3.1. Experimental results

Figs. 9 (a) and (b) present the heave response and the surge force measured for the single PA, respectively. Initially, the employment of the spring PTO leads to a draft increase from 1.15 m to 1.40 m in the equilibrium state, since the spring is pre-tensioned. This small increase in draft leads to a large increase in submerged volume from $1.59\,\mathrm{m}^3$ to $3.77\,\mathrm{m}^3$. This is the main reason for the significant increase in surge force by almost a factor of 2 (see Fig. 9(b)). The heave response is also affected significantly. While the freely floating buoy has a heave RAO close to unity, which is only slightly decreased for the smallest period wave, the heave response of the PA with spring PTO is significantly smaller, ranging between 0.75 and 0.9. Furthermore, a more distinct influence of the incident wave period is visible. For the PA with spring PTO, the decrease in heave response is already apparent at intermediate wave periods with $T < 8$ s.

The wave gauge data is not displayed, since data evaluation indicates in insignificant influence of the PA on the surrounding wave field. This further points to small hydrodynamic interactions between the individual PAs in the wave farm and an emphasis on the mechanical interactions. However, further studies are necessary to determine the influence of different PTO characteristics, since the PTO consisted of a linear spring without a damper in the model tests.

### 3.2. Numerical results

#### 3.2.1. Solo single PA: Calibration

Five different simulation approaches, two in WEC-Sim and three in Ansys AQWA, are compared in Fig. 10, which displays the error $\varepsilon$ (see Eq. (15)) for heave response and surge force. Fig. 10(a) shows a satisfying agreement of the nonlinear AQWA approach with the model test results for the PA's heave response (mean error: −0.27%). Only for the smallest incident wave period, a larger error of - 6.3% is visible. This illustrates that the BEM results and the underlying simplifications (potential flow) are sufficient to model the heave motion of the PA.

Nevertheless, a comparison with other more linear simulation approaches shows the high importance of nonlinear effects. Focusing on the AQWA simulations, the linear AQWA results present an overestimation of roughly 15% for all incident wave periods. For incident wave periods above 6 s, the error of the FA AQWA approach is similar to the error of the linear AQWA approach. However, for shorter period waves the error increases to >20%. Since the difference between these two approaches is the linearization of the buoyancy force via a linear stiffness matrix, these results indicate that this linearization is only valid in long-period waves. Furthermore, the linearization of the Froude–Krylov Force, which is the difference between the nonlinear AQWA approach and the two previously discussed linear approaches, accounts for the constant error of roughly 15%. This importance of nonlinear Froude–Krylov force might mainly originate from the shape of the PA. Especially the PA's shallow draft leads to high changes in submerged PA volume in regular waves, which subsequently necessitates a nonlinear simulation of wave forces.

Focusing on the WEC-Sim results, the fully linear nature of WEC-Sim's implementation becomes apparent, since the linear WEC-Sim results match the FA AQWA results perfectly. To reach a further improvement of the WEC-Sim results, the nonlinear approach was tested, using the same mesh as the AQWA simulations. Nevertheless, the nonlinear WEC-Sim approach did not lead to a significant improvement in the PA's heave response.

For the surge force, similar observations as for the heave response can be made: The fully nonlinear AQWA approach leads to the best results but overestimates the experimental data by roughly 15%. The other approaches, i.e., linear AQWA, linear WEC-Sim, and nonlinear WEC-Sim, show even less agreement with errors of around 30% over all wave periods.

The average heave RAO error is overall lower than the average surge force error. This may originate from the different quantities that are measured: Motion for heave and force for surge. Comparing heave force error and surge force error might lead to similar error levels. However, heave motion is measured, which is affected by further influencing factors, e.g., structural mass, PTO force, and radiation force. The influence of these factors may lead to a higher accuracy in comparing the motion of a floating structure between simulations and experiments than solely comparing the wave force. Furthermore, the larger surge force error might have another origin. Ansys AQWA solves the diffraction problem (i.e., calculating incident wave forces) simulating a fixed structure in waves. However, the buoy is free to move in heave direction in the model tests. This deviation partly leads to the observed overestimation of surge force in the numerical model, since the error reduction from linear to nonlinear AQWA simulations (from roughly 30% to

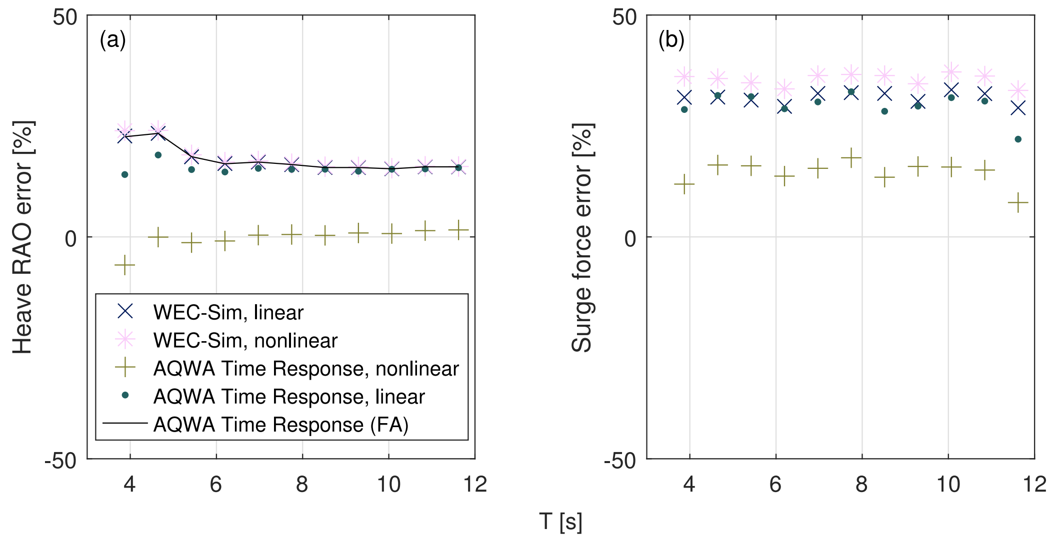


**Fig. 10.** Comparison of numerical results for a single PA from WEC-Sim and AQWA with experimental data: (a) Heave response, (b) Surge force.

15%) indicates a strong influence of nonlinear Froude–Krylov force calculation. This nonlinear Froude–Krylov force calculation respects the instantaneous water surface elevation and the position of the structure. However, the remaining error of 15% indicates that other nonlinearities that are not considered in the simulationsare significant. These could include nonlinear effects in the diffraction force or vortex shedding phenomena that cannot be captured by potential theory simulations. Hence, further studies with higher fidelity approaches are necessary to evaluate these nonlinearities.

Based on the presented results, two main outcomes give directions for the WEC-Sim simulations of the whole wave farm: (1) The BEM data generated by Ansys AQWA is accurate, particularly for the heave DOF, as long as nonlinear effects on buoyancy force and Froude–Krylov force are considered in Ansys AQWA. (2) The nonlinear WEC-Sim model cannot resemble the good performance of the nonlinear Ansys AQWA model. The error identification regarding the nonlinear WEC-Sim approach is not in the scope of this study and remains the subject of future work.

These two outcomes lead to two indications for the application of the BEM data in WEC-Sim: (1) The linear WEC-Sim approach is employed in the following simulations since the nonlinear WEC-Sim approach did not lead to improved results, but only to increased runtime. (2) Due to the deviation between linear WEC-Sim results and experimental data, a calibration is necessary. This calibration aims at minimizing the aforementioned deviation while keeping the resulting PTO force unaffected. Since the PTO force is important for the motion response of the wave farm, its adaptation would lead to subsequent deviations between wave farm simulations and model tests. While an adaptation/increase of the PTO stiffness could lead to a more accurate heave response, this would have made the PTO force less accurate, since the same motion with a higher stiffness leads to higher forces. Furthermore, the surge force would need another adaptation, since it is independent of the PTO settings. Therefore, the PTO stiffness is kept constant and the hydrodynamic data needs to be adapted. It is important to point out that the hydrodynamic data is accurate, as shown by the nonlinear AQWA simulations. However, its adaptation is the only possibility for calibration under the aforementioned restrictions regarding PTO force. Following Eq. (3), three hydrodynamic force components can be adapted: The incident wave force amplitude, the radiation force (by adapting Added mass and Damping), and the buoyancy force (by adapting the linear restoring stiffness). In the following, linear calibration factors for the incident wave force amplitude (for surge and heave motion) are developed, since the motion response is proportional to this quantity. A calibration based on an adaptation of radiation force and/or buoyancy force would also be possible. However, the relation between motion response and these two force components is not as straightforward. Therefore, a more complex identification of calibration factors would be necessary. This is omitted due to the practical necessity of the calibration which accounts for the neglected nonlinear effects in WEC-Sim.

**Table 5**
Mean errors and calibration factors for heave and surge force.

| DOF | Mean error (initial BEM) [%] | Calibration factor [–] |
|---|---|---|
| Surge | 31.42 | 1.3142 |
| Heave | 17.46 | 1.1746 |

In Fig. 11 the non-calibrated and calibrated WEC-Sim results as well as the calibration factors are displayed. The calibration factors for the heave response (Fig. 11(a)) and surge response (Fig. 11(b)) are calculated using the mean error over all wave periods. Table 5 summarizes the mean errors and the subsequent calibration factors.

### 3.2.2. Freely-floating wave farm

To emphasize the importance of the incident wavelength on the wave farm's motion response, all Figures referring to the wave farm use the wavelength $L$ as the $x$-axis.

Applying the now calibrated BEM data to the wave farm, a new BEM simulation was necessary with an adapted water depth of 15 m (for previous single PA simulations: 11.25 m). The previously determined calibration factors are not adapted. Their dependence on water depth is deemed small since they have a linear relation to the PA's motion response and linear theory is used in the numerical modeling.

The freely floating wave farm's motion response in pitch and heave is compared with experimental data in Fig. 12. Both non-calibrated and calibrated data are displayed.

The heave response, which is shown in Fig. 12(a), shows overall good agreement with the experimental data for both simulation approaches with an nRMSE of 0.14. A similar observation can be made for the pitch response (see Fig. 12(b)), which shows sufficient agreement. The calibrated simulations perform slightly better than the non-calibrated simulations, with an nRMSE of 0.16 and 0.2, respectively.

In terms of differences between calibrated and non-calibrated simulations, only for long waves with wavelength $L > 60$ m, the difference is significant, especially in the pitch response. Here, the calibration

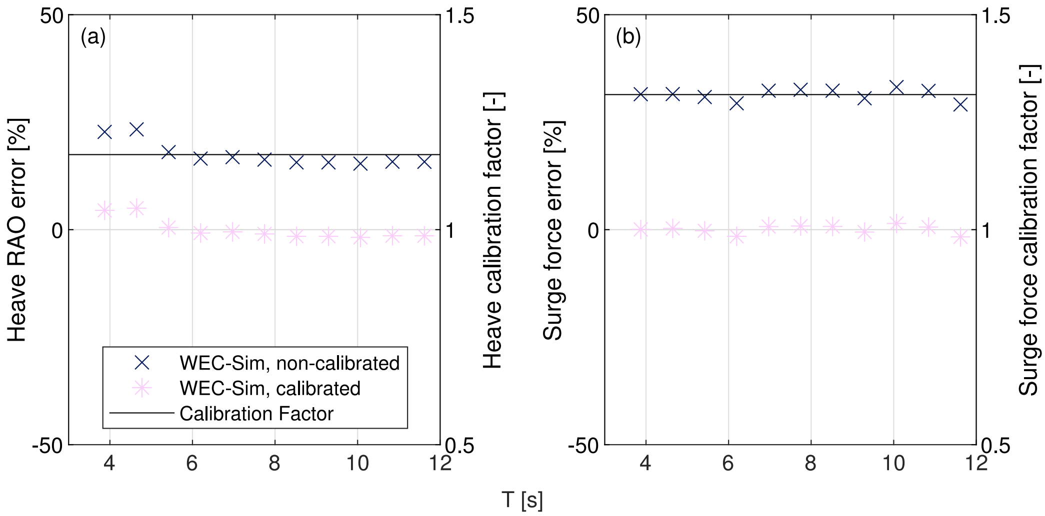


**Fig. 11.** Calibration of WEC-Sim for a single PA based on experimental results: (a) Heave response, (b) Surge force.

has a positive effect on the agreement between simulation and experiment, reducing the nRMSE (for the given wavelength range) from 0.24 (non-calibrated) to 0.15 (calibrated). The overestimation of the single PA's heave response in the non-calibrated simulations also leads to an overestimation of the wave farm's pitch response, which mainly depends on the heave motion of the PA rows with the highest lever arm (rows 1 & 2, see Fig. 1). Furthermore, for the respective wavelength regimes of the heave response, the calibrated simulations show slightly better agreement with the experimental data (nRMSE = 0.11) than the non-calibrated simulations (nRMSE = 0.12).

Analyzing these results, the calibration shows little effect in the shorter wavelengths. Since for wavelengths with $L < L_{Farm}$ (60 m) also hydrodynamic interactions between the PAs have an influence these inaccuracies were expected due to neglecting hydrodynamic interactions. Nevertheless, the mechanical interactions between the PAs are reproduced with good accuracy since the overall shape of the RAOs and their distinctive features (e.g., heave RAO shape between L = 20 and L = 45, heave RAO minimum for L = 75, pitch RAO minimum for L = 50) match the experimental observations. These distinctive features of the RAO originate mainly from the mechanical interactions between the PAs. However, the influence of the hydrodynamic interactions cannot be excluded since the experimental data considers both, mechanical and hydrodynamic coupling effects. Further numerical studies will be necessary to incorporate both effects and quantify their respective importance.

### 3.2.3. Moored wave farm: Non-calibrated

Subsequently, the mooring system is implemented, while respecting the overall accuracy of the calibrated simulations of the freely-floating wave farm (heave: nRMSE = 0.14, pitch: nRMSE = 0.16) as a guideline for the accuracy of the moored wave farm.

The first implementation efforts for the mooring system focused on the lumped-mass mooring model MoorDyn. However, the MoorDyn simulations led to insufficient results, which are most probably originating from the lumped-mass approach in combination with the highly dynamic wave farm. These challenges are depicted with more detail in Appendix A.

To overcome the drawbacks of the lumped-mass approach, the linear mooring matrix approach was used to represent the mooring effects on the wave farm. Since the taut mooring system comprises lines with linear stiffness characteristics, which do not fall slack and are subject to negligible hydrodynamic wave loads due to their small diameter, the application of the linear mooring matrix approach is feasible. In the following paragraphs, two representations of the mooring matrix will be used: Firstly, an initial mooring matrix will be presented, which is adapted to a calibrated mooring matrix in the following steps. Various approaches to the creation of the initial mooring matrix are available, e.g., purely analytical calculations (Amaral et al., 2022), or numerical solutions like MoorPy (Hall et al., 2021). In this study, OrcaFlex is used to generate the initial mooring matrix $C_{m0}$:

$$C_{m0}\left[\frac{kN}{m}\right] = \begin{pmatrix} 136.21 & 0 & 0 & 0 & 159.95 & 0 \\ 0 & 9.49 & 0 & -11.29 & 0 & 0 \\ 0 & 0 & 54.86 & 0 & 0 & 0 \\ 0 & -11.29 & 0 & 20.23 & 0 & 0 \\ 159.95 & 0 & 0 & 0 & 209.92 & 0 \\ 0 & 0 & 0 & 0 & 0 & 22.89 \end{pmatrix}$$

This mooring matrix $C_{m0}$ is valid for the mooring representation of the presented taut mooring system and was created for an origin at $O = (0, 0, 3.6)$, which is the COG of the wave farm's superstructure. Initially, no mooring damping matrix is used. However, the wave farm's response in regular wave simulations showed superharmonic oscillations (i.e., the amplitude spectrum of the respective response has two distinct peaks, one at the wave frequency and another at the system's natural frequency). Hence, a low-level adaptation was implemented by using a surge damping of $10\,\mathrm{N\,s\,m^{-1}}$, which leads to a regular wave farm response in regular waves.

### 3.2.4. Moored wave farm: Calibration

Two calibration methods were employed: A manual calibration and an optimization using a Genetic Algorithm. The manual calibration was reached by manually adapting the mooring matrices until a sufficient agreement with the experimental data was reached. This agreement was quantified using the nRMSE. Additionally, a visual assessment of the RAOs' shape was taken into account. On the contrary, the GA only minimized the nRMSE by adapting the mooring matrices (damping and stiffness). In both matrices, four parameters (diagonal entries for surge, heave, and pitch, as well as surge-pitch coupling entry) need to be optimized, leading to an optimization problem with eight parameters. Since the manual calibration showed that the heave motion is uncoupled from surge and pitch motion, the optimization problem was split to reduce computational cost. One GA was used to optimize heave motion (adapting $C_{m,3,3}$ and $B_{m,3,3}$), while a second GA was used to optimize the surge and pitch motion with six optimization parameters. The fitness score was determined by evaluating Eq. (16) after running regular wave simulations in all 16 wave periods that were investigated in the experiments. The evaluation of one function, i.e., one population (running 16 WEC-Sim calculations, processing results, calculating nRMSE), took roughly 2 min. The GA settings are

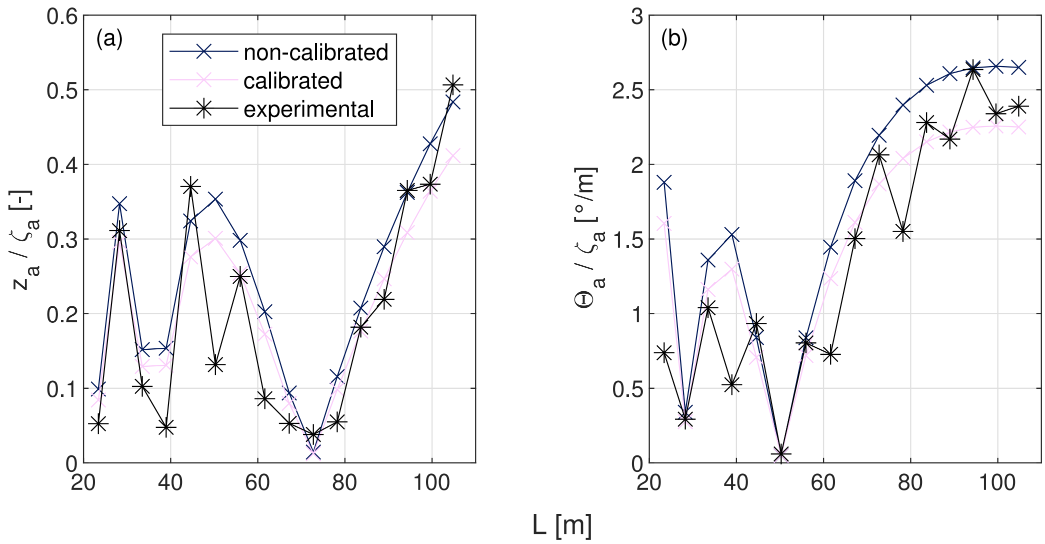


**Fig. 12.** Comparison of the motion response of the freely floating wave farm: (a) Heave response, (b) Pitch response.

**Table 6**
GA settings.

| GA parameter | Value |
|---|---|
| Population Size | 50 |
| Max No. of Generations | 20 |
| Max. No of Stall Generations | 6 |
| Crossover Fraction | 0.8 |

**Table 7**
Parameter Space (Damping is given in prototype scale to improve clarity).

| Optimization parameter | Unit | Lower limit | Upper limit | Step size |
|---|---|---|---|---|
| $F_{1,1}$ | [–] | 0 | 2.0 | 0.1 |
| $F_{3,3}$ | [–] | 0 | 2.0 | 0.1 |
| $F_{5,5}$ | [–] | 0 | 2.0 | 0.1 |
| $F_{5,1}$ | [–] | 0 | 2.0 | 0.1 |
| $B_{m,1,1}$ | [N/(m/s)] | 0 | 100 | 10 |
| $B_{m,3,3}$ | [N/(m/s)] | −100 | 100 | 10 |
| $B_{m,5,5}$ | [N/(m/s)] | 0 | 400 | 10 |
| $B_{m,5,1}$ | [N/(m/s)] | 0 | 200 | 10 |

summarized in Table 6. Discrete values were assigned to the search space of the eight optimization parameters: While absolute values were chosen for the mooring damping matrix, the entries of the mooring stiffness matrix were adapted using a factor between 0 and 2. E.g., for the heave stiffness:

$$C_{m,3,3} = F_{3,3} \cdot C_{m0,3,3} \tag{21}$$

with the heave stiffness factor $F_{3,3}$. The limits and step sizes of the optimization parameters are presented in Table 7. To ensure reasonable results of the GA optimization, a nRMSE equal to 1 was assigned to realizations with unstable simulations (simulation time <preassigned simulation time) or simulations with superharmonic oscillations in the wave farm's responses (two distinct peaks in the response amplitude spectra).

Fig. 13 shows a comparison of the initial settings and the GA calibration with experimental data for the wave farm's heave response. The results of the manual mooring matrix calibration are not shown, since the optimization parameters were not adapted. The calibration of the mooring matrices has little influence on the heave motion of the wave farm since the nRMSE decreases only slightly from 0.2170 to 0.2165. This observation originates from the fact that the mechanical interactions of the PAs, also based on the layout (i.e., distance) of the wave farm, have a much larger influence on the farm's heave motion than the mooring system itself. Subsequently, the mooring stiffness matrix was adapted by a small amount only, while the mooring damping matrix was not adapted at all. The respective values are summarized in Table 8.

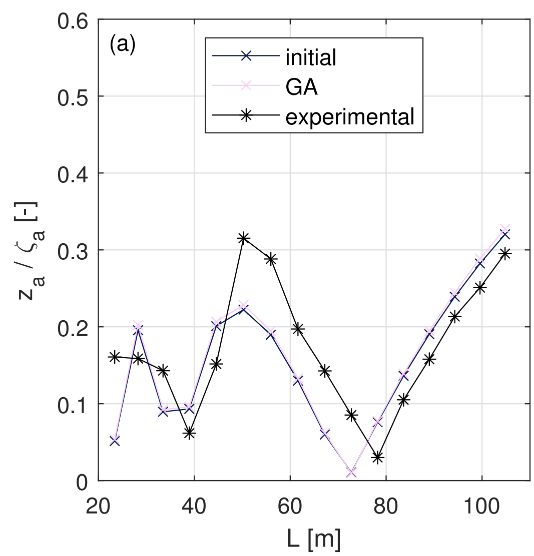


**Fig. 13.** Comparison of the moored wave farm's heave response with different calibration approaches (using linear mooring matrices).

**Table 8**
Results of mooring matrix optimization for the wave farm's heave response.

| Parameter | Unit | Initial | Optimized (GA) |
|---|---|---|---|
| $C_{m,3,3}$ | [kN/m] | 54.86 | 49.37 |
| $D_{m,3,3}$ | [kN/(m/s)] | 0 | 0 |
| nRMSE | [-] | 0.2170 | 0.2165 |

For the calibration of surge and pitch motion, two GA approaches were employed. One approach minimized the nRMSE of the surge and pitch response while the other approach solely minimized the nRMSE of the pitch response. The results of the simulations employing these two GA approaches as well as the initial mooring matrix and the manually calibrated matrices are compared with experimental data in Fig. 14. Fig. 14(a) and (c) show the pitch and surge response of the moored wave farm, while Fig. 14(b) and (d) show the respective responses

 

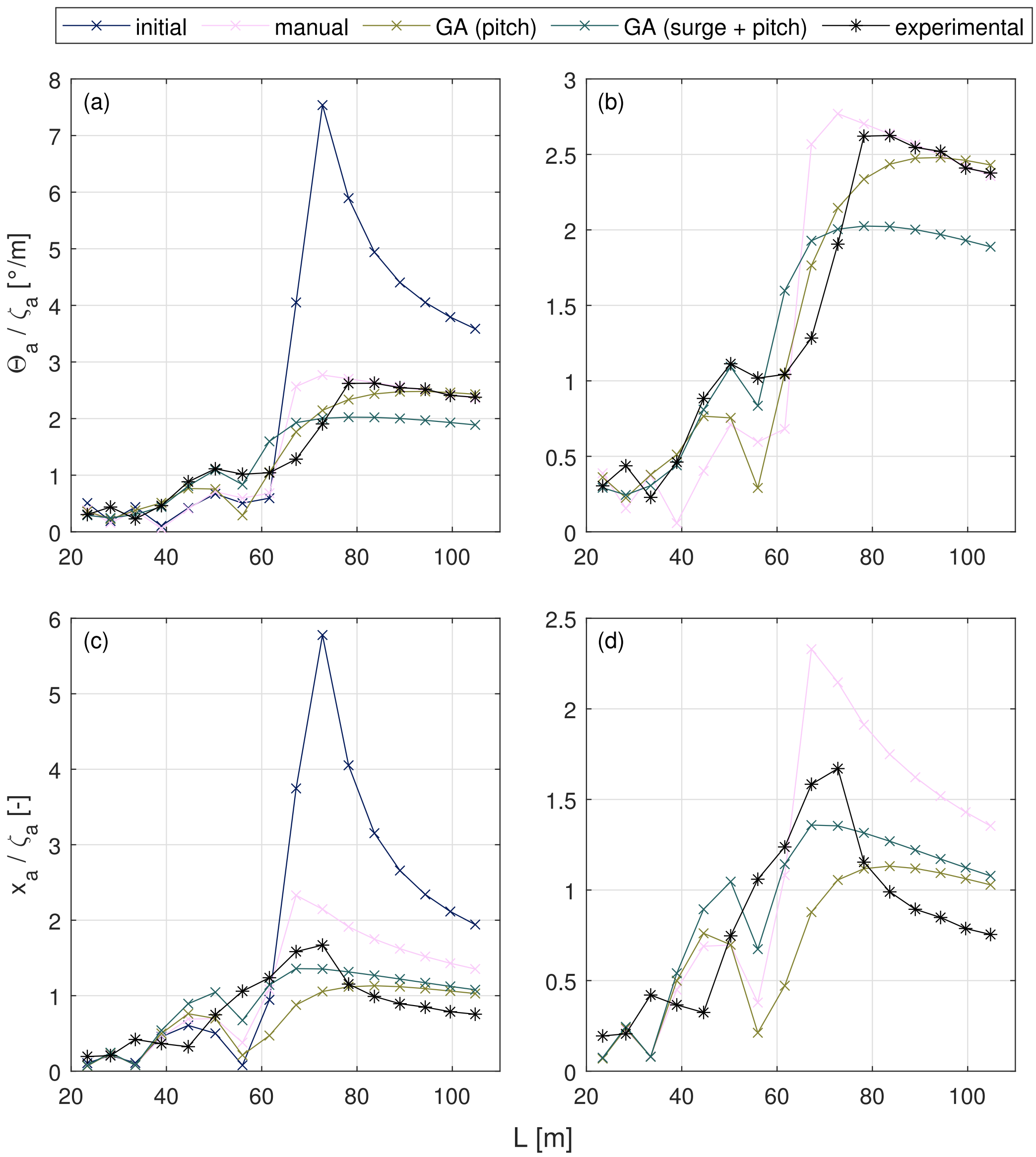


**Fig. 14.** Comparison of the motion response of the moored wave farm with different calibration approaches (using linear mooring matrices): (a) Pitch response, (b) Pitch response (without 'initial' results), (c) Surge response, (d) Surge response (without 'initial' results).

neglecting the results of the initial mooring matrix. Focusing on the results of the initial mooring matrix in Fig. 14(a) and (c), a clear overestimation of the peak response is visible for the pitch response as well as for the surge response. Fig. 14(b) shows that the pitch-optimizing GA and the manual calibration match the experimental pitch response better than the pitch-surge optimizing GA. The pitch-optimizing GA leads to the smallest nRMSE of 0.1125, while the shape of the pitch RAO, especially the sharpness of the peak, is not reproduced. Only manual calibration can reproduce this behavior. However, the resulting nRMSE is 0.1917. The comparison of the surge response, which is presented in Fig. 14(d), shows that none of the calibration approaches can reproduce the moored wave farm's response from physical modeling accurately. The surge-pitch-optimizing GA results in the smallest nRMSE of 0.2018. The mooring matrix entries obtained from the different simulators as well as the resulting nRMSE are summarized in Table 9.

The previously presented results indicate that the mooring system's influence on the wave farm response cannot be represented accurately. The moored wave farm forms a complex dynamic system, which cannot be captured completely by the linear hydrodynamic model in combination with a linear mooring representation. However, recalling the model's accuracy in simulating the freely floating wave farm, which resulted in nRMSE values for the heave and pitch motion of 0.11 and 0.15, respectively, the accuracy of the pitch response has increased to a minimum nRMSE of 0.11, while the accuracy of the heave response has slightly decreased. The absorbed power is chosen as the design factor in this study – referring to an *performance before readiness* approach (Weber, 2012) – and mooring forces are neglected since the presented methodology aims at performance evaluation in early design stages. Since the power absorption of the wave farm has a strong dependence on its pitch motion, the mooring matrices obtained from the pitch-optimizing GA are used as the *calibrated mooring matrices* $C_{m,c}$ and $B_{m,c}$ in the subsequent irregular wave simulations.

$$C_{m,c}\left[\frac{kN}{m}\right] = \begin{pmatrix} 149.83 & 0 & 0 & 0 & 127.96 & 0 \\ 0 & 9.49 & 0 & -11.29 & 0 & 0 \\ 0 & 0 & 54.86 & 0 & 0 & 0 \\ 0 & -11.29 & 0 & 20.23 & 0 & 0 \\ 127.96 & 0 & 0 & 0 & 167.94 & 0 \\ 0 & 0 & 0 & 0 & 0 & 22.89 \end{pmatrix}$$

**Table 9**
Results of mooring matrix optimization for the wave farm's surge and pitch responses.

| Parameter | Unit | Initial | Optimized | | |
|---|---|---|---|---|---|
| | | | Manual | GA (pitch) | GA (pitch, surge) |
| $C_{m,1,1}$ | $\mathrm{kN\,m^{-1}}$ | 136.21 | 136.21 | 149.83 | 149.83 |
| $C_{m,5,5}$ | $\mathrm{kN\,m^{-1}}$ | 209.92 | 335.88 | 167.94 | 455.72 |
| $C_{m,1,5}$ | $\mathrm{kN\,m^{-1}}$ | 159.95 | 159.95 | 127.96 | 175.95 |
| $D_{m,1,1}$ | $\mathrm{kN\,m^{-1}\,s}$ | 0 | 0 | 43.57 | 43.57 |
| $D_{m,5,5}$ | $\mathrm{kN\,m^{-1}\,s}$ | 0 | 174.28 | 305.00 | 270.14 |
| $D_{m,1,5}$ | $\mathrm{kN\,m^{-1}\,s}$ | 0 | 0 | 69.713 | 104.57 |
| nRMSE (Pitch) | – | 0.8458 | 0.1917 | 0.1125 | 0.1682 |
| nRMSE (Surge) | – | 1.1293 | 0.3572 | 0.2839 | 0.2018 |
| nRMSE (mean) | – | 0.9878 | 0.2745 | 0.1982 | 0.1850 |

$$B_{m,c}\left[\frac{kN\,s}{m}\right] = \begin{pmatrix} 43.57 & 0 & 0 & 0 & 69.71 & 0 \\ 0 & 0 & 0 & 0 & 0 & 0 \\ 0 & 0 & 0 & 0 & 0 & 0 \\ 0 & 0 & 0 & 0 & 0 & 0 \\ 69.71 & 0 & 0 & 0 & 305.00 & 0 \\ 0 & 0 & 0 & 0 & 0 & 0 \end{pmatrix}$$

#### 3.2.5. Simulation of realistic sea states

To assess the energy conversion of the wave farm in general and to quantify the importance of model tests for calibration purposes, four sea states were chosen based on scatter data presented by the International Energy Agency (IEA) (Nielsen and Pontes, 2010). Long-crested sea states were used in the scope of this study. However, the numerical model would also allow the simulation of short-crested sea states (e.g., misaligned or spread incident waves), which could be a subject of future studies. Four shallow water test sites were chosen for this study since the water depth in experiments and simulations was set to 15 m. A fully developed sea was simulated as Pierson–Moskowitz (PM) spectra. The sea state with the highest ratio of occurrence was chosen from the respective scatter diagrams. Table 10 summarizes the significant wave height $H_s$ and the peak period $T_p$ of the four sea states, and includes a relative wavelength, which is calculated as the wavelength (linear theory) using $T_p$ divided by the wave farm length of 60 m. Based on the previous experimental findings, short-period waves should lead to a higher energy conversion due to a relative wavelength <0.8.

In the WEC-Sim simulations of the presented sea states, roughly 187 min of real time were simulated (2900 s in model scale). Using the first seven minutes as a warm-up period, the final 180 min were used in the data evaluation to disregard transient effects in the initial phases of the simulation.

Implementing a PI controller with negative PTO stiffness for each PA in the wave farm simulations led to unstable simulations due to the mechanical interactions of all PAs connecting the reactive controllers. This emphasizes the importance of advanced control algorithms for the present wave farm. Existing methods for two-body heaving PAs based on reinforcement learning approaches, e.g., Anderlini et al. (2018), might provide a good starting point.

Due to the instabilities arising from negative PTO stiffness, the PTO stiffness is kept at the constant value from the model tests ($K_{PTO}$ = $9675\,\mathrm{N\,m^{-1}}$) and an optimization of the PTO damping is carried out. The optimization results are presented in Fig. 15. Both, initial and calibrated BEM data are used in this optimization. Using the initial BEM data the PTO power is overestimated by 36% due to the higher heave response of the PA. However, the optimal PTO settings can be found using both. Table 11 summarizes the results of the optimization using the calibrated BEM data, which will be used in the following.

Following the investigation of the optimal PTO settings, the wave farm is simulated in the unmoored state. To avoid excessive motion in the horizontal plane due to the accumulation of numerical errors, a mooring stiffness of $225\,\mathrm{kN\,m^{-1}}$ for surge, sway, and yaw was implemented. Since no coupling with heave and pitch motion is implemented, this does not influence the presented results.

**Table 10**
Irregular wave conditions from wave energy test sites, extracted from data published in Nielsen and Pontes (2010).

| Number | Location | $H_s$ [m] | $T_p$ [s] | $L/L_{Farm}$ |
|---|---|---|---|---|
| SS1 | Galway Bay, Ireland | 0.75 | 4.55 | 0.54 |
| SS2 | Hanstholm, Denmark | 1.00 | 5.00 | 0.64 |
| SS3 | Port Kembla, Australia | 0.88 | 9.92 | 1.80 |
| SS4 | Pilot zone, Portugal | 1.25 | 8.75 | 1.54 |

**Table 11**
Optimal PTO settings and subsequent power output for a solo single PA with constant PTO stiffness of $K_{PTO}$ = $9675\,\mathrm{N\,m^{-1}}$.

| | $C_{PTO,opt}$ [kN(m/s)] | $P_{max}$ [kW] |
|---|---|---|
| SS1 | 52.29 | 0.93 |
| SS2 | 57.51 | 1.72 |
| SS3 | 125.49 | 1.20 |
| SS4 | 109.80 | 2.58 |

The results of the total converted energy are presented in Fig. 16. Again, simulations with initial and calibrated BEM data are compared, showing a clear overestimation of the converted energy using the initial BEM data. This overestimation has a constant factor of 36% for all sea states. Due to the linear model, the same constant factor as in the single PA simulations applies.

Table 12 compares the average absorbed power per PA of the unmoored wave farm and the single PA (see Fig. 15), as well as the ratio between the two values. This resembles the q-factor that is frequently used in assessing wave farm performance:

$$q = \frac{P_{farm}}{\sum P_{single}} \tag{22}$$

with the wave farm's absorbed power $P_{farm}$ and the absorbed power of a single WEC $P_{single}$.

The q-factor is usually applied to evaluate hydrodynamic interactions in wave farms. In this study, this evaluation is not made on the farm level, but on a single device level to focus on the effects the mechanical coupling of the PAs has on their performance. In simple terms, the factor presented in Table 12 estimates the performance loss due to this mechanical connection in comparison to individually deployed PAs. This performance loss should be balanced with less CAPEX due to reduced mooring costs and installation costs, finally leading to decreased LCOE. While this holistic assessment of the total wave farm costs and the comparison to the deployment of individual PAs is not in the scope of the present study, it emphasizes that WEC-Sim simulations can help assess the wave farm performance and the influence of the mechanical coupling on this performance.

A clear difference between SS1 & SS2 (low peak period) and SS3 & SS4 (large peak period) can be observed. While the mechanically coupled PAs can reach at least 70% of the solo single PA's potential in the former two sea states, the factor is below 30% for the latter two sea states. This emphasizes the experimental findings, furthermore

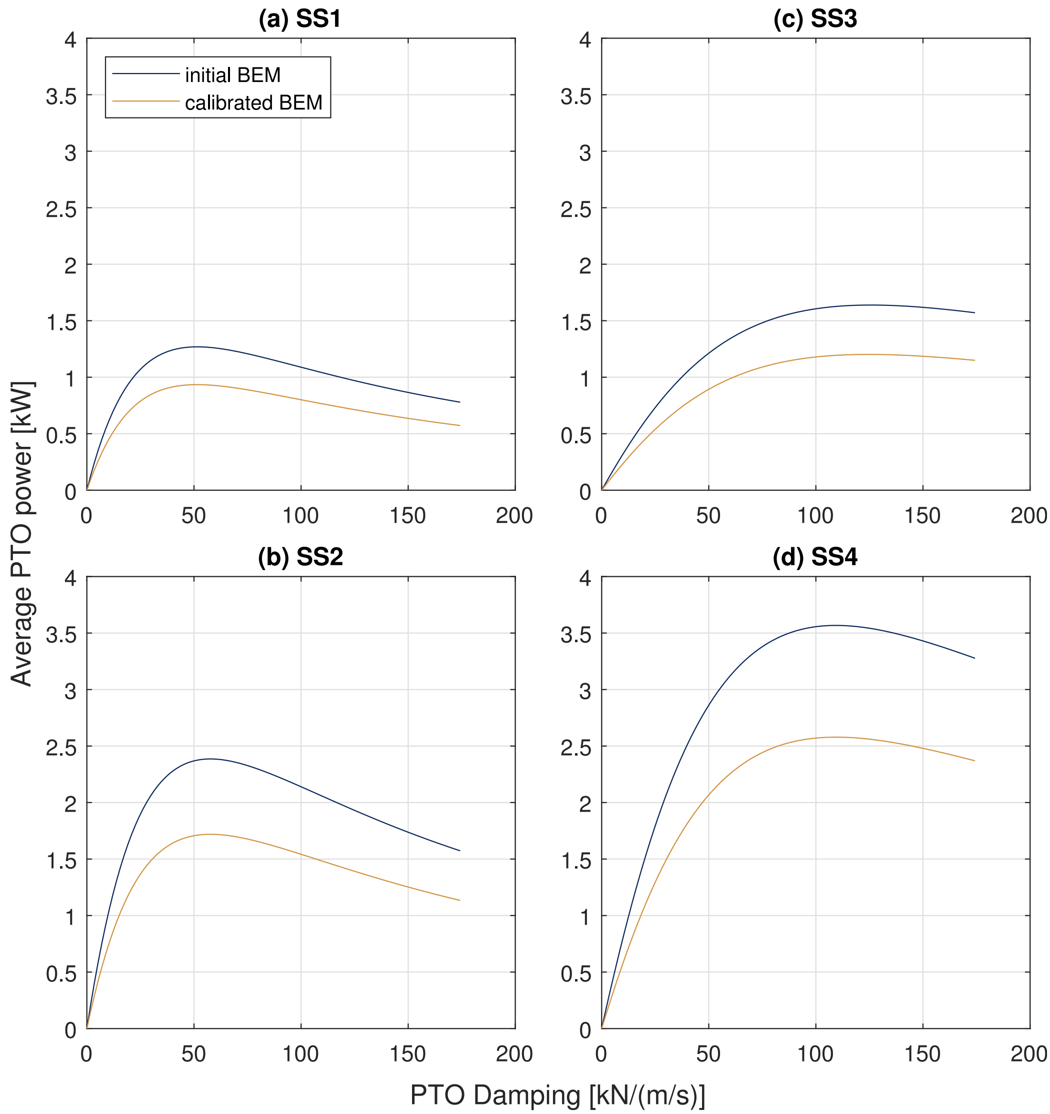


**Fig. 15.** Average absorbed power as a function of PTO damping with a constant PTO stiffness of $k = 9675\,\mathrm{N\,m^{-1}}$ (reactive control) for a single PA.

**Table 12**
Comparison of mean absorbed power per PA [kW] for the solo single PA and the unmoored wave farm.

| | Absorbed Power per PA [kW] | | Factor [%] |
|---|---|---|---|
| | Solo single PA | Wave farm | |
| SS1 | 0.93 | 0.72 | 77 |
| SS2 | 1.72 | 1.21 | 70 |
| SS3 | 1.20 | 0.24 | 20 |
| SS4 | 2.58 | 0.71 | 28 |

**Table 13**
Comparison of mean absorbed power per PA [kW] for the wave farm (calibrated BEM data).

| | Absorbed power per PA [kW] | | |
|---|---|---|---|
| | Calibrated mooring | Uncalibrated mooring | No mooring |
| SS1 | 0.72 | 0.72 | 0.72 |
| SS2 | 1.22 | 1.22 | 1.21 |
| SS3 | 0.24 | 0.24 | 0.24 |
| SS4 | 0.72 | 0.72 | 0.71 |

pointing out that the wave farm's operation is only efficient in waves with a wavelength shorter than the overall length of the wave farm.

Table 13 compares the mean absorbed power per PA for three different cases: Wave farm with initial mooring, wave farm with calibrated mooring, and wave farm without mooring. The results given in the Table highlight a minimal influence of mooring calibration on the absorbed power.

Fig. 16 as well as Tables 12 and 13, emphasize that the calibration of the BEM data has a much more significant influence on the converted energy than the calibration of the mooring system. The mooring influence is in the same order of magnitude as in the previous experimental study (Meyer et al., 2023), which also indicated only a small difference in motion response between unmoored and taut-moored wave farm.

## 4. Conclusion

This paper presents findings on the accuracy of modeling approaches for wave farms in the early design stages. Model test results of a single PA are presented and used to calibrate the WEC-Sim model of a single PA, based on BEM data generated using Ansys AQWA. After this calibration, the wave farm is simulated in WEC-Sim. At first, the unmoored wave farm is simulated, showing good agreement between simulations and previously published experimental data. The

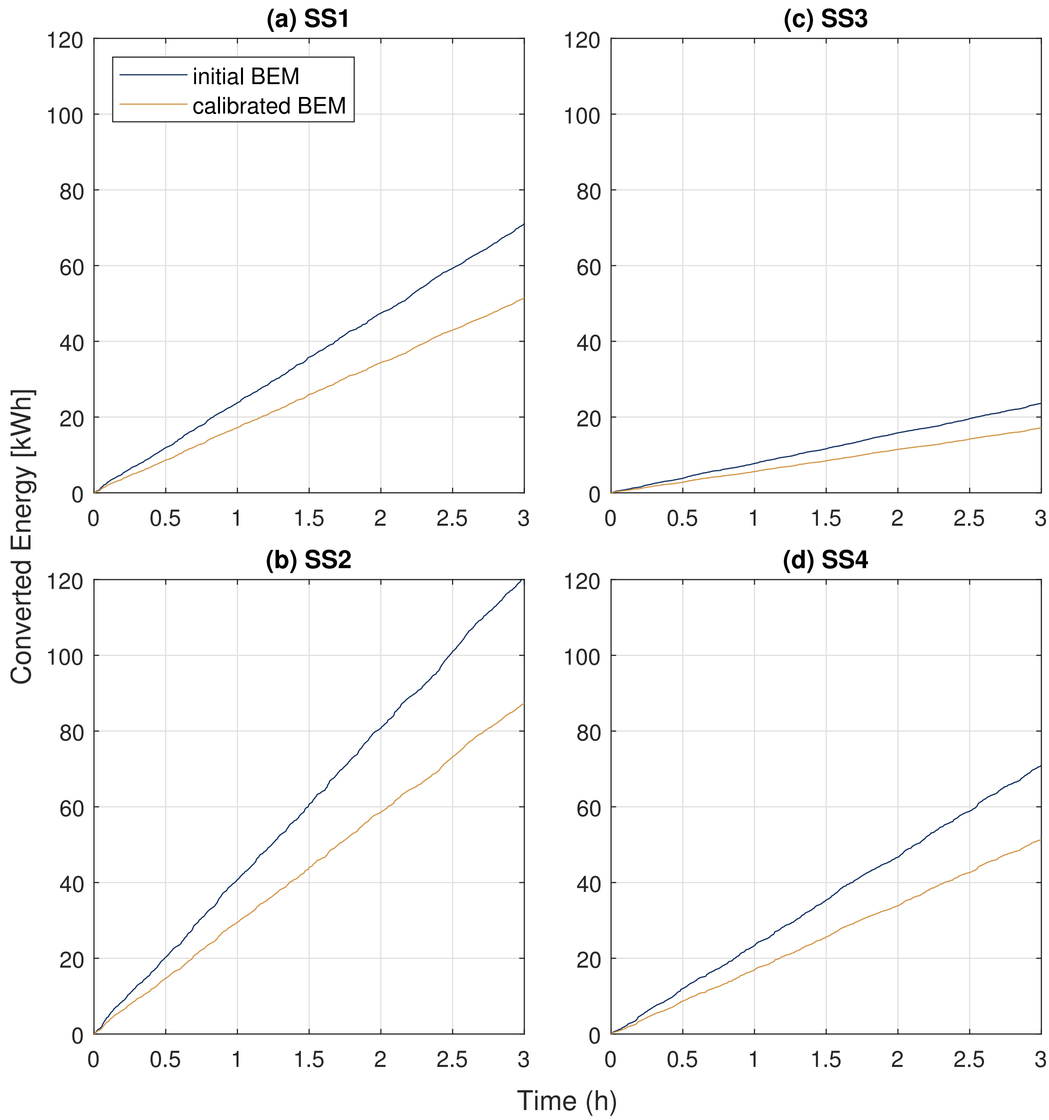


**Fig. 16.** Comparison of the converted energy of the unmoored wave farm: (a) SS1, (b) SS2, (c) SS3, (d) SS4.

moored wave farm was subsequently simulated, and the mooring system based on linear mooring matrices was calibrated using model test data. Finally, simulations in irregular sea states were carried out. Initially, optimal PTO properties were found using Exhaustive Search optimization. These optimal PTO settings were then used to determine the converted energy.

The key findings of this study are:

- The mechanical interactions of the complex wave farm at hand are reproduced with high accuracy by WEC-Sim. Hence, the first insights in the initial design phases can be gained without extensive high-fidelity modeling (physical model tests, CFD).
- BEM simulations are sufficient as input data, but calibration is necessary for an accurate estimation of wave farm performance.
- For the mechanically coupled wave farm used in this study, the mechanical interactions are of much higher importance for power output than the mooring interaction. Hence, the mooring system can be simplified to model the wave farm for power conversion assessments in the early design stages.
- Subsequently, the calibration of BEM data has a much higher influence on the evaluation properties (i.e., converted energy) than the calibration of the mooring system. Therefore, for an accurate determination of wave farm performance, single PA model tests (focusing on the motion response in waves) should be prioritized over tests of the whole wave farm in the planning of model test campaigns for early design stages.
- The main findings of the previous experimental study (Meyer et al., 2023) without PTO damping are confirmed: The wave farm operates best in incident waves with a length shorter than the wave farm's length.

Summarizing these findings, the calibration of the BEM data based on single PA model tests has much more influence on the design factors (i.e., converted energy of the wave farm) than the mooring calibration based on the extensive model tests of the complete wave farm. Therefore, an accurate determination of the mechanical interactions in the wave farm as well as the power output can be achieved by employing mid-fidelity models. However, the aspects that are neglected in the present methodology, i.e., the hydrodynamic interaction between the individual PAs in the wave farm, should be respected when other wave farm designs are evaluated. E.g., for wave farms with significantly smaller separation distances between the PAs, a stronger focus should be laid on the evaluation of the hydrodynamic interactions. Further high-fidelity studies will be necessary to investigate the correlation between wave farm layout and the subsequent emphasis on mechanical or hydrodynamic interactions between the PAs. Similarly, for wave farms with different PA shapes, the hydrodynamic interactions should be observed. Since according to the proposed approach, single PA model tests are recommended, possible hydrodynamic interactions should be considered, e.g., by a careful evaluation of the wave field in the vicinity of the PA. Finally, a third point to be considered in this regard is the influence of the PTO settings on the hydrodynamic interactions in the farm.

Furthermore, mooring forces were not used as a design factor in this study, and mooring design can be crucial in the design of a complete structure (wave farm, FOWT, etc.). Based on the lower accuracy in the moored wave farm's simulations, physical model tests of a whole wave farm play a key role in the mooring design. While the problems in mooring simulations may originate from the dynamic characteristics of the complete wave farm, they however point out that further research in this area is necessary, and currently, model tests are indispensable. Similarly, the surge force error observed in the initial BEM simulations indicates that approaches with higher fidelity are necessary.

Finally, the extent of model tests also correlates with the design phase of the wave farm. In the early design stages, the converted energy of a wave farm concept may be design driving to increase TPL as proposed by Weber (2012), and numerical simulations for design validation or layout optimization are carried out. Hence, in this design stage, single PA model tests are more cost-efficient than testing the whole wave farm. Additionally, the BEM data calibration could be achieved, at least for the present test case, using the BEM model by calibrating the WEC-Sim input data using the AQWA Time Domain results. In summary, the present study indicates that the combination of single PA model tests and mid-fidelity modeling in WEC-Sim is a feasible approach – while keeping the aforementioned limitations concerning hydrodynamic interactions in mind – for early design stages. Afterwards, more complex model tests of the wave farm using the now validated wave farm design with fixed system fundamentals can be carried out for mooring design, not only focusing on operational conditions but also on survival conditions with more nonlinear sea states. In this scope, advanced control systems could also be investigated. The results of the present study indicate that improved controllers could increase wave farm performance significantly.

## CRediT authorship contribution statement

**Jannik Meyer:** Writing – original draft, Writing – review & editing, Methodology, Investigation, Formal analysis, Conceptualization. **Christian Windt:** Writing – review & editing, Supervision, Methodology, Conceptualization. **Arndt Hildebrandt:** Resources, Project administration, Funding acquisition, Conceptualization, Supervision, Writing – review & editing. **Torsten Schlurmann:** Conceptualization, Funding acquisition, Project administration, Resources, Supervision, Writing – review & editing.

## Declaration of competing interest

The authors declare that they have no known competing financial interests or personal relationships that could have appeared to influence the work reported in this paper.

## Data availability

Data will be made available on request.

## Acknowledgments

This work has been supported by the Deutsche Forschungsgemeinschaft (DFG, German Research Foundation) – SFB1463 – 434502799.

The authors would like to acknowledge the important support of the technical staff of Ludwig-Franzius-Institute during the model test campaigns. Furthermore, we would like to thank the student researchers Anna-Lena Wolters, Malte Schmidt and Henrik Neufeldt for their valuable simulation work in the scope of their student theses at Ludwig-Franzius-Institute.

The scientific color map *Batlow* (Crameri, 2021) is used in this study to prevent visual distortion of the data and exclusion of readers with colourvision deficiencies (Crameri et al., 2020).

## Appendix A. Lumped-mass mooring models in the simulation of highly dynamic wave farms with taut line mooring systems

As mentioned in Section 3.2.3, the simulation of the moored wave farm using MoorDyn, which is a lumped-mass mooring model, led to various problems. In the following, these problems are highlighted in more detail. To emphasize that the issues are not inherent to MoorDyn but originate from the lumped-mass approach, further simulations with the industry model OrcaFlex (OF) are presented. This Appendix aims to provide further research directions for high-fidelity mooring models (compared to the low-fidelity approach of the linear mooring matrices, which were employed in the present study).

In this Appendix, only the uncalibrated BEM data is used in both models. Firstly, the good agreement between OrcaFlex and WEC-Sim for the single PA and the freely-floating wave farm is shown to emphasize the accurate simulation of the PA hydrodynamics and their mechanical interaction in both models. Secondly, the moored wave farm is simulated and the respective results of both simulation models are presented.

The simulation results of both, OF and WEC-Sim, for single PA and freely-floating wave farm are presented in Fig. A.17. The response of the single PA is simulated with nearly no difference (rms = 0.002). Similarly, the heave and pitch response of the freely-floating wave farm shows only a few differences, mainly in the area of short waves with L <60. Here, the different approaches of OF and WEC-Sim concerning the wave field might become apparent: In WEC-Sim the wave excitation force is calculated using the phase shift based on the position of the floating structure (in this manuscript, the subsequent adaptation for different PAs is achieved using Eq. (20)), using only one distinct wave elevation in the whole field. On the contrary, the wave elevation is calculated over the whole domain in OF. However, the heave and pitch response of the freely-floating wave farm are very similar for both, OF and WEC-Sim, with a rms of 0.043 for heave and $0.0657\,^\circ\,\mathrm{m}^{-1}$ for pitch. These small differences show that both models are capable of simulating the PA hydrodynamics and their mechanical coupling with similar accuracy.

However, implementing the taut mooring lines for the wave farm using the lumped-mass approach inherent to MoorDyn and OF leads to strongly increasing errors. Fig. A.18 shows the heave and pitch response of the wave farm. Here, both responses show minor differences between both models, which may further originate from the different implementations of the lumped-mass approach. While the wavelength of the maximum is estimated accurately by the simulations, its amplitude is significantly overestimated. While the maximum value differs for OF ($6.47\,^\circ\,\mathrm{m}^{-1}$) and WEC-Sim ($8.56\,^\circ\,\mathrm{m}^{-1}$), the overestimation of the experimental values is clear for both models.

Extensive efforts to calibrate MoorDyn were undertaken. An artificial damping term could be adapted in MoorDyn to reduce the overestimation. Nevertheless, this increase in damping leads to further problems, i.e. an increase in pitch response in shorter wavelengths between $L > 40$ m and $L < 60$ m. Furthermore, the damping increase led to increasing runtimes, since larger damping requires smaller

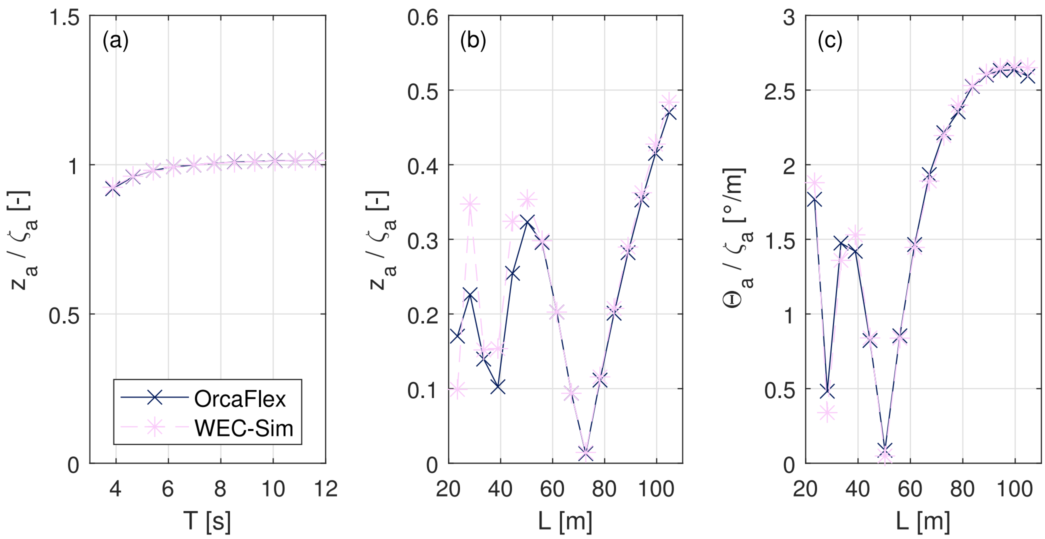


**Fig. A.17.** Comparison of the motion response of single PA and freely-floating wave farm: (a) Heave response of single PA, (b) Heave response of wave farm, (c) Pitch response of wave farm.

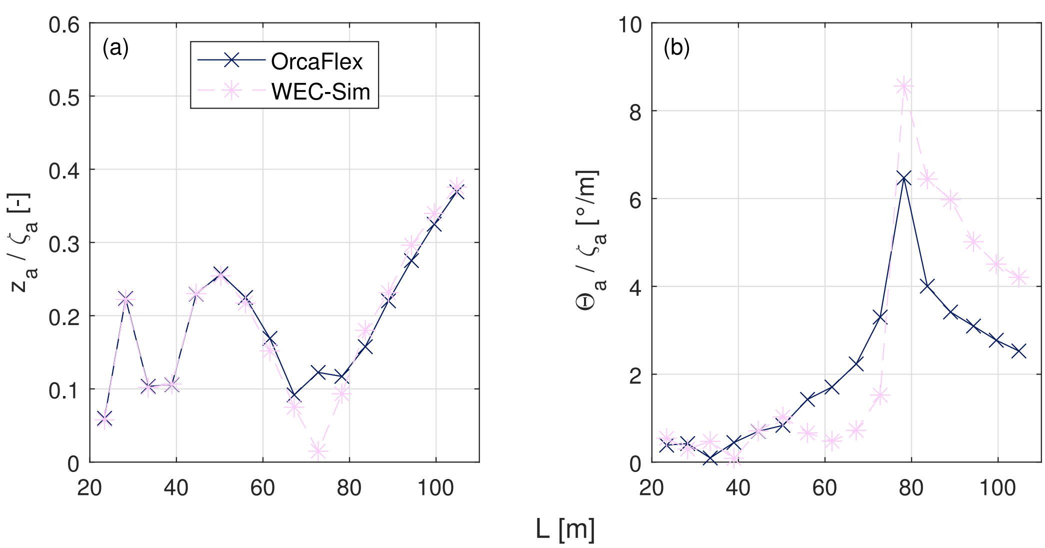


**Fig. A.18.** Comparison of the motion response of moored wave farm: (a) Heave response, (b) Pitch response.

timesteps for stable simulations. However, no convergence towards the experimental data could be achieved. Hence, further research on lumped-mass mooring models is necessary to improve the models' performance applied to highly dynamic wave farms with taut mooring system.

## Appendix B. Simulink diagrams

See Fig. B.19.

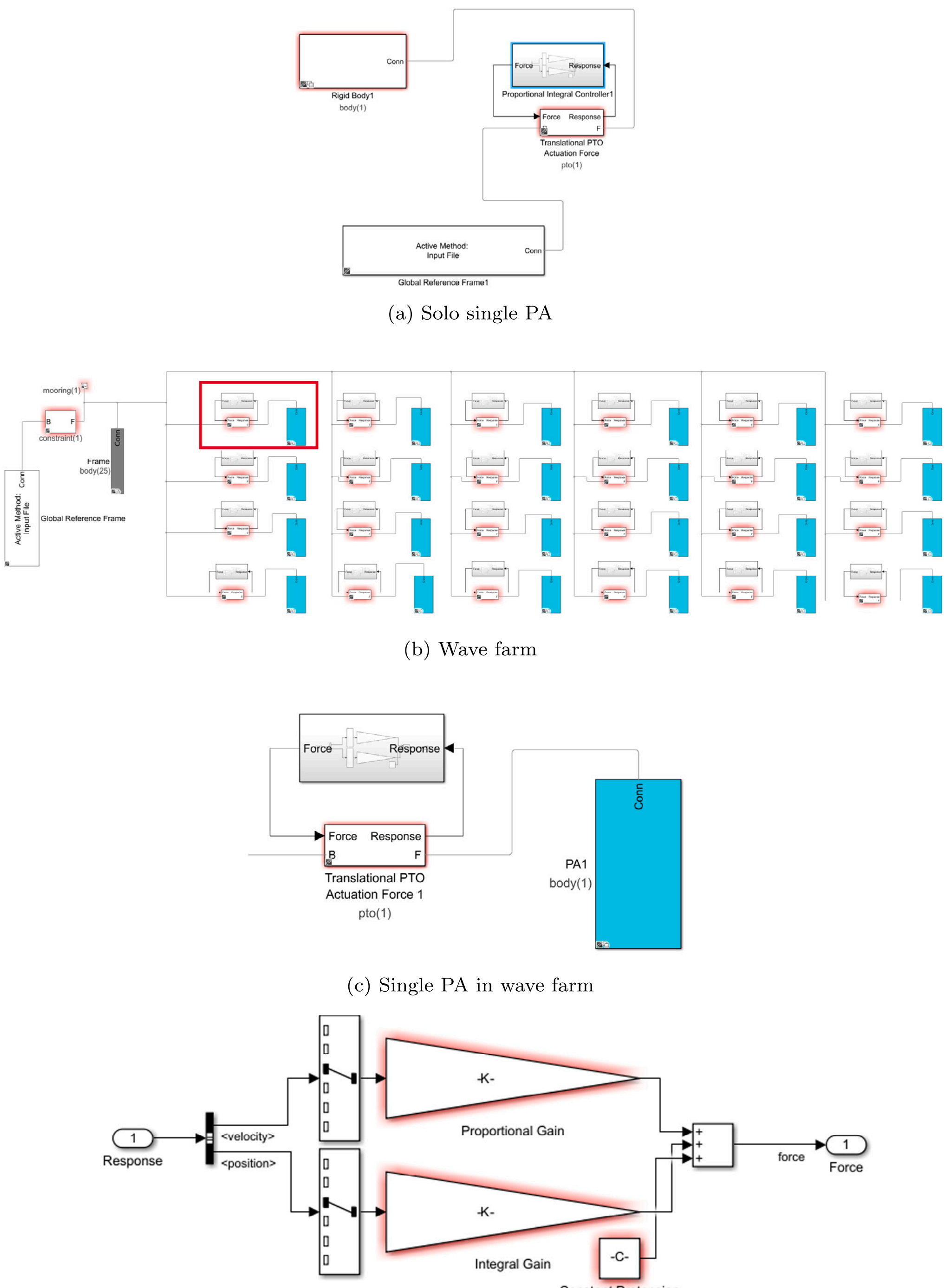


(a) Solo single PA

(b) Wave farm

(c) Single PA in wave farm

(d) Controller

**Fig. B.19.** Simulink models: (a) Solo single PA, (b) Wave farm, (c) Single PA in wave farm, (d) Controller.

## References


Amaral, G.A., Pesce, C.P., Franzini, G.R., 2022. Mooring system stiffness: A six-degree-of-freedom closed-form analytical formulation. Mar. Struct. 84, 103189. http://dx.doi.org/10.1016/j.marstruc.2022.103189.

Anderlini, E., Forehand, D., Bannon, E., Xiao, Q., Abusara, M., 2018. Reactive control of a two-body point absorber using reinforcement learning. Ocean Eng. 148, 650–658. http://dx.doi.org/10.1016/j.oceaneng.2017.08.017.

ANSYS, 2022. AQWA theory manual.

Babarit, A., 2013. On the park effect in arrays of oscillating wave energy converters. Renew. Energy 58, 68–78. http://dx.doi.org/10.1016/j.renene.2013.03.008.

Balitsky, P., Quartier, N., Fernandez, G.V., Stratigaki, V., Troch, P., Verao Fernandez, G., Stratigaki, V., Troch, P., 2018. Analyzing the near-field effects and the power production of an array of heaving cylindrical WECs and OSWECs using a coupled hydrodynamic-pto model. Energies 11 (12), http://dx.doi.org/10.3390/en11123489.

Balitsky, P., Quartier, N., Stratigaki, V., Verao Fernandez, G., Vasarmidis, P., Troch, P., 2019. Analysing the near-field effects and the power production of near-shore WEC array using a new wave-to-wire model. Water 11 (6), 1137. http://dx.doi.org/10.3390/w11061137.

Bozzi, S., Giassi, M., Miquel, A.M., Antonini, A., Bizzozero, F., Gruosso, G., Archetti, R., Passoni, G., 2017. Wave energy farm design in real wave climates: the Italian offshore. Energy 122, 378–389. http://dx.doi.org/10.1016/j.energy.2017.01.094.

Cao, F., Han, M., Shi, H., Li, M., Liu, Z., 2022. Comparative study on metaheuristic algorithms for optimising wave energy converters. Ocean Eng. 247, http://dx.doi.org/10.1016/j.oceaneng.2021.110461.

Clemente, D., Rosa-Santos, P., Taveira-Pinto, F., 2021. On the potential synergies and applications of wave energy converters: A review. Renew. Sustain. Energy Rev. 135, 110162. http://dx.doi.org/10.1016/j.rser.2020.110162.

Crameri, F., 2021. Scientific colour maps. http://dx.doi.org/10.5281/zenodo.5501399.

Crameri, F., Shephard, G.E., Heron, P.J., 2020. The misuse of colour in science communication. Nat. Commun. 11 (1), 1–10. http://dx.doi.org/10.1038/s41467-020-19160-7.

Cummins, W.E., 1962. The impulse response function and ship motions. Technical Report, David Taylor Model Basin Washington DC, pp. 101–109.

Devolder, B., Stratigaki, V., Troch, P., Rauwoens, P., 2018. CFD simulations of floating point absorber wave energy converter arrays subjected to regular waves. Energies 11 (3), 641. http://dx.doi.org/10.3390/en11030641.

Domínguez, J.M., Crespo, A.J., Hall, M., Altomare, C., Wu, M., Stratigaki, V., Troch, P., Cappietti, L., Gómez-Gesteira, M., 2019. SPH simulation of floating structures with moorings. Coast. Eng. 153, 103560. http://dx.doi.org/10.1016/j.coastaleng.2019.103560.

European Commission, 2020. An EU strategy to harness the potential of offshore renewable energy for a climate neutral future. URL https://eur-lex.europa.eu/legal-content/EN/TXT/?uri=COM:2020:741:FIN, COM/2020/741.

Faedo, N., Peña-Sanchez, Y., Pasta, E., Papini, G., Mosquera, F.D., Ferri, F., 2023. SWELL: An open-access experimental dataset for arrays of wave energy conversion systems. Renew. Energy 212, 699–716. http://dx.doi.org/10.1016/j.renene.2023.05.069.

Faraggiana, E., Chapman, J., Williams, A., Whitlam, C., Masters, I., 2022. Investigation of new layout design concepts of an array-on-device WaveSub device. Renew. Energy 190, 501–523. http://dx.doi.org/10.1016/j.renene.2022.03.126.

Gong, H., Shi, H., Han, Z., Cao, F., 2022. Experimental and numerical investigation on an optimization method of heaving buoy wave energy converter arrays based on a given target wave spectrum. Ocean Eng. 259, 111766. http://dx.doi.org/10.1016/j.oceaneng.2022.111766.

Gunn, K., Stock-Williams, C., 2012. Quantifying the global wave power resource. Renew. Energy 44, 296–304. http://dx.doi.org/10.1016/j.renene.2012.01.101.

Hall, M., 2021. Moordyn v1.01.02. URL https://github.com/FloatingArrayDesign/MoorDyn/releases/tag/v1.01.02.

Hall, M., Goupee, A., 2015. Validation of a lumped-mass mooring line model with DeepCwind semisubmersible model test data. Ocean Eng. 104, 590–603. http://dx.doi.org/10.1016/j.oceaneng.2015.05.035.

Hall, M., Housner, S., Sirnivas, S., Wilson, S., 2021. Moorpy (quasi-static mooring analysis in python). http://dx.doi.org/10.11578/dc.20210726.1.

Han, M., Cao, F., Shi, H., Kou, H., Gong, H., Wang, C., 2023a. Parametrical study on an array of point absorber wave energy converters. Ocean Eng. 272, http://dx.doi.org/10.1016/j.oceaneng.2023.113857.

Han, M., Cao, F., Shi, H., Zhu, K., Dong, X., Li, D., 2023b. Layout optimisation of the two-body heaving wave energy converter array. Renew. Energy 205 (January), 410–431. http://dx.doi.org/10.1016/j.renene.2023.01.100.

He, G., Luan, Z., Zhang, W., He, R., Liu, C., Yang, K., Yang, C., Jing, P., Zhang, Z., 2023. Review on research approaches for multi-point absorber wave energy converters. Renew. Energy 119237. http://dx.doi.org/10.1016/j.renene.2023.119237.

Kristiansen, E., Hjulstad, Å., Egeland, O., 2005. State-space representation of radiation forces in time-domain vessel models. Ocean Eng. 32 (17–18), 2195–2216. http://dx.doi.org/10.1016/j.oceaneng.2005.02.009.

Kung, S.-Y., 1978. A new identification and model reduction algorithm via singular value decomposition. In: Proc. 12th Asilomar Conf. on Circuits, Systems and Computer. pp. 705–714. http://dx.doi.org/10.1299/kikaic.64.1970.

Lamont-Kane, P., 2015. Physical and Numerical Modelling of Wave Energy Converter Arrays (Ph.D. thesis). Queen's University of Belfast.

Li, X., Xiao, Q., Zhou, Y., Ning, D., Incecik, A., Nicoll, R., McDonald, A., Campbell, D., 2022. Coupled CFD-mbd numerical modeling of a mechanically coupled wec array. Ocean Eng. 256, http://dx.doi.org/10.1016/j.oceaneng.2022.111541.

Meyer, J., Windt, C., Sinn, P., Hildebrandt, A., 2023. On the mooring methodology of heaving point absorber arrays. Ocean Eng. 281, 114659. http://dx.doi.org/10.1016/j.oceaneng.2023.114659.

Mork, G., Barstow, S., Kabuth, A., Pontes, M.T., 2010. Assessing the global wave energy potential. In: International Conference on Offshore Mechanics and Arctic Engineering. 49118, pp. 447–454. http://dx.doi.org/10.1115/OMAE2010-20473.

Nielsen, K., 2010. Report T02-0.0: Development of recommended practices for testing and evaluating ocean energy systems. OES-IA Annex II Extension Summary Report.

Nielsen, K., Pontes, T., 2010. Report T02-1.1 - OES IA annex II task 1.2 generic and site-related wave energy data.

NREL & Sandia, 2023. WEC-Sim theory manual. URL https://wec-sim.github.io/WEC-Sim/main/theory/index.html. (Accessed on 08 August 2023).

Ogden, D., Ruehl, K., Yu, Y.-H., Keester, A., Forbush, D., Leon, J., Tom, N., 2022. Review of WEC-sim development and applications. Int. Marine Energy J. 5 (3), 293–303. http://dx.doi.org/10.36688/imej.5.293-303.

Papillon, L., Costello, R., Ringwood, J.V., 2020. Boundary element and integral methods in potential flow theory: a review with a focus on wave energy applications. J. Ocean Eng. Mar. Energy 6 (3), 303–337. http://dx.doi.org/10.1007/s40722-020-00175-7.

Pecher, A., Kofoed, J.P., 2017. Handbook of ocean wave energy. Springer Nature.

Penalba, M., Davidson, J., Windt, C., Ringwood, J.V., 2018. A high-fidelity wave-to-wire simulation platform for wave energy converters: Coupled numerical wave tank and power take-off models. Appl. Energy 226, 655–669. http://dx.doi.org/10.1016/j.apenergy.2018.06.008.

Rollano, F.T., Tran, T.T., Yu, Y.-H.H., García-Medina, G., Yang, Z., 2020. Influence of time and frequency domain wave forcing on the power estimation of a wave energy converter array. J. Marine Sci. Eng. 8, http://dx.doi.org/10.3390/jmse8030171.

Ruehl, K., Ogden, D., Yu, Y.-H., Keester, A., Tom, N., Forbush, D., Leon, J., Grasberger, J., Husain, S., 2022. WEC-Sim v5.0.1. Zenodo, http://dx.doi.org/10.5281/zenodo.7121186, URL https://zenodo.org/badge/latestdoi/20451353.

Rusu, L., Rusu, E., 2021. Evaluation of the worldwide wave energy distribution based on ERA5 data and altimeter measurements. Energies 14 (2), 394. http://dx.doi.org/10.3390/en14020394.

Sinn, P., 2016. Vergleich einer neuartigen Wellenkraftwerkstechnologie mit existierenden Stromversorgungsmöglichkeiten an einem dezentralen Modellstandort (Ph.D. thesis). Technische Universität München.

Sirnivas, S., Yu, Y.-H., Hall, M., Bosma, B., 2016. Coupled mooring analyses for the wec-sim wave energy converter design tool. In: International Conference on Offshore Mechanics and Arctic Engineering, Vol. 49972. American Society of Mechanical Engineers, V006T09A023. http://dx.doi.org/10.1115/OMAE2016-54789.

Stratigaki, V., Troch, P., Forehand, D., Stallard, T., Kofoed, J., Folley, M., Benoit, M., Babarit, A., Kirkegaard, J., Gallach-Sánchez, D., Bosscher, L., Rauwoens, P., Elsäßer, B., Lamont-Kane, P., Mccallum, P., Mcnatt, C., Angelelli, E., Pecher, A., Carpintero Moreno, E., Vantorre, M., 2014a. Physical modelling of wave energy converter arrays in a large-scale wave basin: the WECwakes project. In: Proceedings of the HYDRALAB IV Joint User Meeting, Lisbon, July 2014, Vol. 1.

Stratigaki, V., Troch, P., Stallard, T., Forehand, D., Kofoed, J.P., Folley, M., Benoit, M., Babarit, A., Kirkegaard, J., 2014b. Wave basin experiments with large wave energy converter arrays to study interactions between the converters and effects on other users in the sea and the coastal area. Energies 7 (2), 701–734. http://dx.doi.org/10.3390/en7020701.

Taghipour, R., Perez, T., Moan, T., 2008. Hybrid frequency–time domain models for dynamic response analysis of marine structures. Ocean Eng. 35 (7), 685–705. http://dx.doi.org/10.1016/j.oceaneng.2007.11.002.

Teixeira-Duarte, F., Clemente, D., Giannini, G., Rosa-Santos, P., Taveira-Pinto, F., 2022. Review on layout optimization strategies of offshore parks for wave energy converters. Renew. Sustain. Energy Rev. 163, http://dx.doi.org/10.1016/j.rser.2022.112513.

Weber, J., 2012. WEC technology readiness and performance matrix–finding the best research technology development trajectory. In: Proceedings of the 4th International Conference on Ocean Energy, Dublin, Ireland, Vol. 17.

Yang, B., Wu, S., Zhang, H., Liu, B., Shu, H., Shan, J., Ren, Y., Yao, W., 2022. Wave energy converter array layout optimization: A critical and comprehensive overview. Renew. Sustain. Energy Rev. 167, http://dx.doi.org/10.1016/j.rser.2022.112668.

Zeng, X., Wang, Q., Kang, Y., Yu, F., 2022. Hydrodynamic interactions among wave energy converter array and a hierarchical genetic algorithm for layout optimization. Ocean Eng. 256, 111521. http://dx.doi.org/10.1016/j.oceaneng.2022.111521.

Zhu, K., Shi, H., Han, M., Cao, F., 2022. Layout study of wave energy converter arrays by an artificial neural network and adaptive genetic algorithm. Ocean Eng. 260, http://dx.doi.org/10.1016/j.oceaneng.2022.112072.